A Novel Parameter Estimation Method of Motion Error in Terahertz SAR Imaging Based on Viterbi and RANSAC Algorithms

Siyu Chen and Yong Wang, *Senior Member, IEEE*

***Abstract*—Terahertz synthetic aperture radar (THz SAR) imaging has gradually become one of the hotspots with the development of THz technology. The wide bandwidth can provide satisfactory resolution in the SAR imaging, whereas the small wavelength makes the imaging system more sensitive to the platform vibration error (VE), which may seriously affect its image quality. In this article, a novel parameters estimation method of motion error in the THz SAR imaging based on the Viterbi algorithm (VA) and random sample consensus (RANSAC) algorithm is proposed. First, the VA is employed to extract the instantaneous frequency (IF) introduced by the platform VE. The VA is defined based on the generalization of IF characteristics, and it further considers the relationship between the frequency points at adjacent time points based on the maximum value search in the time–frequency representation, which makes it perform well in the IF extraction. Second, the RANSAC algorithm in conjunction with the nonlinear least square (NLS) algorithm and the minimum-entropy principle is proposed to perform the VE parameters estimation. Due to the noise or the platform velocity variation, there will exist the points that deviate from the high-frequency VE, which can be mitigated via the combination of the RANSAC algorithm and the NLS technique. Simultaneously, the well-focused THz SAR imaging results can be acquired after compensating via the best parameter estimation results selected by the minimum-entropy principle. Finally, the validity of the proposed method has been demonstrated through the simulation and real-measured experiments.**

***Index Terms*—Platform vibration error (VE) compensation, random sample consensus (RANSAC) algorithm, terahertz synthetic aperture radar (THz SAR), Viterbi algorithm (VA).**

I. Introduction

TERAHERTZ (THz) technology has attracted more and more attention due to its unique performance in various fields currently. The THz wave lies between the millimeter wave and the infrared wave, and its wavelength covers the electromagnetic radiation region from 0.03 to 3 mm [1], [2]. The THz technology has many unique advantages, such as narrow beam, large bandwidth, strong penetration, and anti-interference characteristics, which make it have great application potential [3], [4], [5], [6], [7]. Simultaneously, the ultrahigh resolution radar systems are more and more widely used in the imaging field [8], [9], [10], [11], [12], which can be achieved by the THz technique more easily. Therefore, the THz technology is commonly used in the field of synthetic aperture radar (SAR) imaging [13], [14], [15].

However, the THz wave still has some limits. First, the absorption spectrum of water vapor, oxygen, and other substances present in the troposphere in large quantities will cause serious attenuation of THz waves. Moreover, at lower altitudes, the presence of large particles, such as sand and dust in the atmosphere, will also cause scattering of THz waves and thus cause non-negligible attenuation of THz wave transmission. Second, the large bandwidth of the THz system needs to be achieved via the frequency multiplication, so THz systems are complex and difficult to implement. Third, the devices of the THz system are expensive, which leads to the limitations in its development.

Nevertheless, compared with the microwave SAR system, the THz SAR system can achieve higher resolution and shorter imaging period [16]. Furthermore, since the imaging system of THz SAR has stronger penetration ability, it can still obtain the imaging results normally in the environment with smoke or haze. Hence, the imaging technology of THz SAR is a new radar technology with great development potential.

There are still some problems to be solved in the THz SAR imaging process. On account of the small wavelength, the platform vibration error (VE) in THz SAR systems will blur the images along the azimuth direction seriously [17]. Hence, the research for the platform VE compensation is indispensable. It has been demonstrated that this platform VE is modeled in the form of the harmonic motion [18]. Therefore, the hybrid linear frequency modulation–sinusoidal frequency modulation (SFM) signal [19] is introduced to formulate the received signals of the THz SAR system. Nevertheless, the instantaneous frequency (IF) of the received signals includes the information of the platform VE, but it cannot be used for compensation directly. Hence, after the IF extraction, the vibration parameters, especially the vibration frequencies, need to be further estimated for the compensation. Due to the noise or the platform velocity variation, the IF extraction and the parameter estimation accuracy will be affected. Therefore, it is of great importance to investigate the

Manuscript received 13 July 2023; revised 20 November 2023 and 7 July 2024; accepted 3 August 2024. Date of publication 8 August 2024; date of current version 26 August 2024. This work was supported by the National Science Fund for Distinguished Young Scholars under Grant 62325104. *(Corresponding author: Yong Wang.)*

The authors are with the Research Institute of Electronic Engineering Technology, Harbin Institute of Technology, Harbin 150001, China (e-mail: 21b905043@stu.hit.edu.cn; wangyong6012@hit.edu.cn).

Digital Object Identifier 10.1109/JSTARS.2024.3440221

high precision IF extraction and the VE estimation in THz SAR imaging process.

At present, there have been many researches on platform VE compensation. In [20], the parameter estimation approach based on the inverse radon transform is proposed for the VE estimation. Moreover, the wavelet reconstruction is introduced for THz SAR imaging in [21]. Nevertheless, the wavelet-based method is inapplicable to the conditions with complicated VE. In [22], the local fractional Fourier transform (LFrFT)-based method can be used for compensating in THz SAR imaging process. However, the LFrFT-based method requires the existence of dominant scattering points in the radar scenario, and is useful for compensating the monocomponent VE. The above methods are applicable to the compensation of THz SAR imaging with simple VE. But in practice, there may exist more complex VE, which should be further studied.

Currently, some scholars have discussed the compensation algorithms in the case of complex VE. In [23] and [24], the discrete sinusoid frequency modulation transform is proposed for the parameter estimation of the SFM signal, and it is improved via the optimization algorithm. In [25] and [26], the chirplet decomposition method is introduced for compensating the VE. Additionally, the SFM Fourier transform-based algorithm is used to reconstruct the phase error of the THz SAR system in [27]. And in [28], the linear chirplet transform and the empirical mode decomposition are employed to focus the imaging results, which can suppress the defocus along azimuth direction.

Based on the above analysis, many scholars have studied the IF extraction and parameter estimation in the VE compensation of the THz system, but there still exist many problems to be studied. First, the IF of the radar return can be extracted through the time–frequency (TF) analysis method, such as the TF ridge extraction [29]. However, when there are multiple point targets in the THz SAR imaging scene, the TF distribution characteristics in the TF representation of the received signals are more complex, which will reduce the accuracy of the IF extraction in the case of no isolated strong scattering point. Based on this issue, the Viterbi algorithm (VA) is introduced for IF extraction in this article. The VA is defined by generalizing the characteristics of IF in the TF representation, and it can extract the IF in multipoint target imaging scenarios lacking isolated strong scattering points.

Second, due to the noise, there will exist the frequency points that are not belonging to the VE in the extracted IF, which will reduce the accuracy. Moreover, when the platform velocity varies, the frequency points in the extracted IF may deviate from the high-frequency VE, which will also affect the parameter estimation effect. Therefore, the random sample consensus (RANSAC) algorithm combined with the nonlinear least square (NLS) algorithm is introduced for the parameter estimation after the IF extraction in this article. The RANSAC algorithm can exclude the outliers introduced by the noise or the platform velocity variation. Hence, the inliers belonging to the high-frequency VE are selected for parameter estimation, which improves the accuracy of parameter estimation.

Third, after the iteration of the RANSAC algorithm, we should select the best fitting model for the compensation, so the judgment principle after the iteration is vital. Moreover, the ultimate goal of high-frequency VE compensation is to obtain the well-focused imaging results. Therefore, we introduce the minimum-entropy principle to choose the best fitting model after the iteration in this article. In this way, the most suitable VE estimation model can be acquired, and the well-focused imaging results can be obtained.

Fourth, the procedures of the VE compensation in this article include the IF extraction and the VE estimation. Therefore, the VA and the RANSAC algorithm are combined for the VE compensation in this article. After the IF extraction via the VA, the RANSAC algorithm can further reduce the impact of noise, as well as the estimation error of the previous step algorithm, namely, the IF extraction. Hence, the combination of these two algorithms can further reduce the impact of the noise on the compensation and improve the accuracy of the parameter estimation.

To sum up, in this article, the VA and the RANSAC algorithm are introduced to extract IF and estimate VE for compensation in THz SAR imaging process. The VA can extract the IF with high precision in multipoint target imaging scenarios lacking isolated strong scattering points. Additionally, the RANSAC algorithm can mitigate the interference of the points that are not belonging to the high-frequency VE, so we combine both the RANSAC method and NLS algorithm to estimate the vibration parameters accurately in the presence of noise or platform velocity variation. Meanwhile, since the purpose of vibration parameter estimation is to obtain the well-focused imaging results, the minimum-entropy principle is combined with the RANSAC algorithm to select the best estimation of the vibration parameter. Based on the best parameter estimation result, the defocus along the azimuth direction can be further restrained by constructing the compensation function.

The main contributions are as follows.

1) When there exist multiple point targets but no isolated strong scattering point in the THz SAR imaging scenario, the accuracy of the IF extraction will be affected. Therefore, the VA algorithm is introduced for the VE compensation of THz SAR, which is defined based on the generalization of IF characteristics, so it can extract IF with noise or in multipoint target imaging scenarios lacking isolated strong scattering points.
2) Due to the noise or the platform velocity variation, there will exist points in the extracted IF that deviate from the high-frequency VE, which will affect the parameter estimation accuracy of the VE in THz SAR. Therefore, the RANSAC algorithm is introduced in combination with the NLS algorithm, which can exclude the outliers introduced by the noise or the platform velocity variation, and select the inliers belonging to the high-frequency VE for the parameter estimation. So the RANSAC algorithm can accurately estimate the platform high-frequency VE of THz SAR even in the presence of noise or platform velocity variation.
3) Since the best fitting model needs to be selected for compensation after the iteration, and the purpose of the VE compensation for THz SAR is to obtain the well-focused

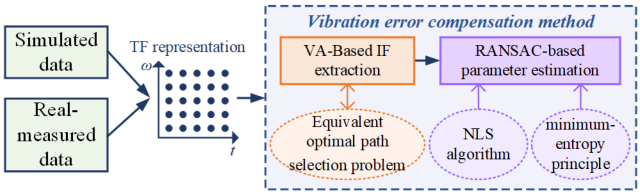

Fig. 1. Overview of our main work.

imaging results, the minimum-entropy principle is introduced into the RANSAC algorithm as the judgment principle. Through the minimum-entropy principle, the best fitting model can be selected for the VE compensation, and the focused THz SAR imaging results can be obtained.

4) Aiming at the VE compensation of the THz SAR imaging, our proposed method combines the VA with the RANSAC algorithm for the IF extraction and the VE estimation. After the IF extraction via the VA, the RANSAC algorithm can further reduce the impact of noise and the error of the IF extraction. Hence, combining these two algorithms can further suppress the defocus of the imaging results in the presence of noise.

Fig. 1 describes our main work. The rest of this article is organized as follows. In Section II, we establish the signal model of the THz SAR with high-frequency VE. Section III discusses the proposed VE compensation method in detail. The effectiveness and performance advantages of the method are investigated by both the simulation and real-measured experiments in Section IV. Finally, Section V concludes this article.

II. THz SAR Imaging Model With High-Frequency Vibration Error of the Platform

In order to study the VE compensation in the THz SAR imaging process, the corresponding geometric model is established at first. Due to the small wavelength of THz SAR, the imaging scene width of THz SAR is typically small. As shown in Fig. 2, the solid blue line represents the real platform movement track, while the red dotted line corresponds to the ideal platform movement track. The THz SAR system works at the vertical side-looking mode, moving along the X-axis at velocity V and height H.

Assume that the transmitted signal is a chirp signal. After demodulating, the echo signal for a point target N is formulated by

$$s(t_m,\tau) = w_r(\tau-\tau_0)\,w_a(t_m-t_n) \times \exp\left[j\pi K_r\left(\tau-\frac{2R_N(t_m)}{C}\right)^2 - j\frac{4\pi}{\lambda}R_N(t_m)\right] \quad (1)$$

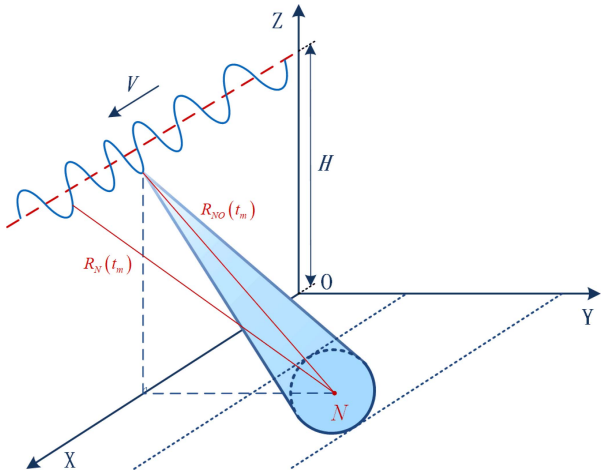

Fig. 2. Geometric model of THz SAR imaging.

where $\tau_0 = \frac{2R_N(t_m)}{C}$, t_m means the slow time, τ represents the fast time, $R_N(t_m)$ indicates the slant range from target N to the actual antenna phase center, C is light speed, t_n represents zero doppler time, the frequency modulation rate K_r indicates the ratio of the bandwidth B to the pulsewidth, and λ is the transmitted wavelength.

Then, the range compression is performed on the received signal, which is shown as

$$s(t_m,\tau) = w_a(t_m-t_n) \times \mathrm{sinc}\left[\pi B\left(\tau-\frac{2R_N(t_m)}{C}\right)\right] \times \exp\left[-j\frac{4\pi}{\lambda}R_N(t_m)\right]. \quad (2)$$

On account of the small wavelength of THz SAR, the platform VE cannot be ignored. The actual VE satisfies the Dirichlet conditions, hence, the VE is established as harmonic motion [30], which is denoted as

$$\Delta R_r = \sum_{j=1}^{J} \alpha'_j \sin(2\pi\eta_j t_m + \phi_j) \quad (3)$$

where $j = 1, 2, \ldots, J$, α'_j, η_j, and ϕ_j are the vibration amplitude, frequency, and initial phase, respectively.

Currently, the research in [31] demonstrates that the imaging quality is barely influenced by the platform VE along the platform movement direction (namely the X-axis). Moreover, the uneven sampling errors along the platform movement direction can be eliminated through the devices like GPS [28]. Hence, we mainly consider the VE of the other two axes in this article. Therefore, the VE in (3) can be decomposed as

$$\begin{cases} \Delta R_Y = \Delta R_r \sin(\delta) \\ \Delta R_Z = \Delta R_r \cos(\delta) \end{cases} \quad (4)$$

where δ is the angle between the VE and Z-axis.

For the point target $N(X_N, Y_N, 0)$, the slant range $R_N(t_m)$ is indicated as

$$R_N(t_m) = \left[(Vt_m - X_N)^2 + (\Delta R_Y - Y_N)^2 + (\Delta R_Z + H)^2\right]^{1/2}. \tag{5}$$

Then, the Taylor expansion is performed on (5), and the slant range is rewritten as follows:

$$R_{NO} = \left(Y_N^2 + H^2\right)^{1/2} \tag{6}$$

$$\begin{aligned} R_N(t_m) &\approx R_{NO} + \frac{(Vt_m)^2}{2R_{NO}} - \frac{X_N V t_m}{R_{NO}} + \frac{X_N^2}{2R_{NO}} + \Delta R \\ &= R_{NO} + \frac{(Vt_m)^2}{2R_{NO}} - \frac{X_N V t_m}{R_{NO}} + \frac{X_N^2}{2R_{NO}} \\ &\quad + \frac{\Delta R_Z H - \Delta R_Y Y_N}{R_{NO}} \\ &= R_{NO} + \frac{(Vt_m)^2}{2R_{NO}} - \frac{X_N V t_m}{R_{NO}} + \frac{X_N^2}{2R_{NO}} \\ &\quad + \sum_{j=1}^{J} \alpha_j \sin(2\pi\eta_j t_m + \phi_j). \end{aligned} \tag{7}$$

After the range compression, the range cell migration (RCM) needs to be further compensated. On the one hand, related studies in [31] and [32] demonstrate that the amplitude of the high-frequency VE in the THz SAR is typically millimetric. On the other hand, $H/R_{NO} < 1$ and $Y_N/R_{NO} < 1$. Consequently, the amplitude of the term ΔR in the RCM introduced by the high-frequency VE is only a few millimeters. Moreover, in the simulated and real-measured THz SAR system of this article, the range resolution ρ_r is 3.75 and 3.125 cm, respectively. Therefore, the amplitude of ΔR is less than $\rho_r/4$. Additionally, due to the millimetric VE, $2\Delta R/C \approx 0$, so the RCM introduced via the high-frequency VE can be ignored in the sinc function envelope of (2). Therefore, the RCM caused by the high-frequency VE can be neglected. Then, the compensation function $\exp\left\{j\pi f_a^2 f_r^2 / K_a f_c^2 \left[\sqrt{1-\left(\frac{\lambda f_a}{2V}\right)^2}\right]^3 - j\pi f_a^2 f_r / K_a f_c\right\}$ is constructed for the range cell migration correction (RCMC), where f_a is the Doppler frequency, f_r means the range frequency, and f_c represents the carrier frequency. After multiplying with the compensation function in the range-Doppler domain, the RCMC is finished and the radar return is indicated as

$$\begin{aligned} s(t_m, \tau) &= w_a(t_m - t_n) \times \operatorname{sinc}\left[\pi B\left(\tau - \frac{2R_{NO}}{C}\right)\right] \\ &\quad \times \exp\left[j\left(\pi K_a t_m^2 + 4\pi\frac{X_N V}{\lambda R_{NO}} t_m - 2\pi\frac{X_N^2}{\lambda R_{NO}} \right.\right. \\ &\quad \left.\left. -4\pi\frac{R_{NO}}{\lambda}\right)\right] \\ &\quad \times \exp\left[j\left(-\frac{4\pi}{\lambda}\sum_{j=1}^{J}\alpha_j \sin(2\pi\eta_j t_m + \phi_j)\right)\right] \end{aligned} \tag{8}$$

where $K_a = -\frac{2V^2}{\lambda R_{NO}}$ denotes the Doppler frequency modulation.

Then, by multiplying with the compensation function in (9), we can obtain (10).

$$s_{\text{ref}}(t_m) = \exp\left(-j\pi K_a t_m^2\right) \tag{9}$$

$$\begin{aligned} s(t_m, \tau) &= w_a(t_m - t_n) \times \operatorname{sinc}\left[\pi B\left(\tau - \frac{2R_{NO}}{C}\right)\right] \\ &\quad \times \exp\left[j\left(4\pi\frac{X_N V}{\lambda R_{NO}} t_m - 2\pi\frac{X_N^2}{\lambda R_{NO}} - 4\pi\frac{R_{NO}}{\lambda}\right)\right] \\ &\quad \times \exp\left[j\left(-\frac{4\pi}{\lambda}\sum_{j=1}^{J}\alpha_j \sin(2\pi\eta_j t_m + \phi_j)\right)\right]. \end{aligned} \tag{10}$$

From (10), we can see that the VE introduces the phase error $-\frac{4\pi}{\lambda}\sum_{j=1}^{J}\alpha_j \sin(2\pi\eta_j t_m + \phi_j)$ into the received signals. Hence, the effect of the phase error on the received signals depends mainly on the ratio of α_j to λ. The amplitude of the platform VE in the THz SAR system is common only to a few millimeters. Moreover, the wavelength of the THz SAR is from 0.03 to 3 mm. From the above, it can be seen that the amplitude of the platform VE is usually in the same order of magnitude as the wavelength of the THz SAR. Therefore, in the THz SAR system, the high-frequency VE of the platform cannot be neglected, and its compensation should be carefully considered.

In this section, we establish the THz SAR imaging model with the high-frequency VE. Specifically, the platform VE is modeled as the harmonic motion, thus introducing the phase error into the radar echo in the form of sinusoidal modulation. Furthermore, the VE cannot be ignored in the THz SAR imaging because of its small wavelength. Thus, the VE needs to be reconstructed to focus the images via the VE compensation.

III. Platform Vibration Error Reconstruction Method

A. Viterbi Algorithm

The high-frequency VE of the platform can introduce the sinusoidal modulation phase error into the received signals. So the extraction of the phase error is key for compensation. Through taking the logarithm, the phase error can be extracted, but it may lead to the phase-shift ambiguity. Hence, the VE cannot be obtained accurately from the phase in this case. Since the IF, namely the derivative of phase, also contain the information of the VE, we extract the IF instead of the phase to obtain the accurate VE information. Through the VA, the IF including the VE information can be extracted, and then the VE parameters can be estimated via the RANSAC algorithm. Based on the above processing, the VE can be reconstructed without phase-shift

ambiguity, then the defocus in the THz SAR imaging can be suppressed.

From (10), we can see that the IF of the received signal is sinusoidal modulated, which is represented as

$$\omega_{\text{real}}(t_m) = \frac{d\phi_{\text{real}}(t_m)}{dt_m} = \frac{4\pi X_N V}{\lambda R_{NO}} - \frac{4\pi}{\lambda}\sum_{j=1}^{J} 2\pi \cdot \alpha_j \eta_j \cos(2\pi\eta_j t_m + \phi_j) \tag{11}$$

where $\phi_{\text{real}}(t_m)$ means the phase of (10).

In order to acquire IF via VA, the short-time Fourier transform (STFT) is employed for obtaining TF representation at first. The STFT-based TF representation can be indicated as $\text{STFT}(m,\omega)$, where m is the discrete slow time and ω denotes the frequency.

Then, we arrange the TF representation $\text{STFT}(m,\omega)$ in the nonincreasing order based on its amplitude. ω_m^r is the discrete frequency point in the TF representation at the time m, $r = 1, 2, \ldots, R$, and R represents the number of frequency points at the time m. After sorting via the nonincreasing order, the position of ω_m^r in the nonincreasing sequence is denoted by a_r.

For the THz SAR VE compensation, VA is introduced with the purpose of extracting the IF from TF representation. The TF representation contains the IF information, where these IF points manifest as distinct and relatively large points. Due to the noise or other interference, the IF points may not be the absolute maximum points but are one of the maximum values in the TF representation. Additionally, the IF in the echo signal varies continuously with the slow time, so in the discrete TF representation, the IF between two consecutive slow time points changes a little. The IF extraction is to find a continuous path in TF representation, which passes through these relatively large points. Based on the above analysis, to accurately extract the IF, it is necessary to ensure continuity between the points while finding these relatively large points in the TF representation. To solve the above problem, we establish the following two hypotheses to generalize the IF characteristics for the construction of the VA.

1) At time m, the corresponding IF value should be one of the maximum values in the TF representation.
2) The IF corresponding to the two consecutive slow time points have little change.

These two hypothesis conditions generalize the characteristics of IF in the TF representation. Thus, by meeting these conditions, IF can be accurately extracted via the VA. Based on the above two hypotheses, the nonincreasing penalty function $\vartheta(x)$ and the nondecreasing penalty function $\chi(x,y)$ are defined to form the VA, shown as follows:

$$\begin{cases} \vartheta(\text{STFT}(m,\omega_m^r)) = a_r - 1 \\ \chi(x,y) = \begin{cases} 0, & |x-y| \le \Delta \\ c(|x-y| - \Delta), & |x-y| > \Delta \end{cases} \end{cases} \tag{12}$$

where c means the weight of the penalty function and Δ represents the threshold.

Hence, the VA-based IF estimation [33] can be represented as the sum of $\vartheta(x)$ and $\chi(x,y)$, which is expressed via

$$\hat{\omega}_{\text{est}}(m) = \arg\min_{g(m)\in G}\left\{\sum_{m=m_1}^{m_L}\vartheta(\text{STFT}(m,g(m))) + \sum_{m=m_1}^{m_L-1}\chi(g(m),g(m+1))\right\} \tag{13}$$

where $m = m_1, m_2, \ldots, m_l, \ldots, m_L$ denotes the discrete slow time, L is the number of the discrete time, $g(m)$ means the path, and G represents all paths between m_1 and m_L.

In the VA-based IF estimation process, the penalty function $\vartheta(x)$ ranks the discrete TF distribution based on the amplitude, primarily aiming to achieve the first hypothesis. $\vartheta(x)$ can acquire the extreme points in the TF representation, which are the most likely IF points. Furthermore, based on the second hypothesis, the penalty function $\chi(x,y)$ is constructed with the aim of ensuring the continuity of the extracted IF, thereby mitigating the impact of noise or other interference. When $\Delta \to \infty$, the IF estimation can be equivalent to the STFT maximum search, that is, the TF ridge extraction. By selecting the appropriate value of c and Δ, IF can be extracted with better accuracy. Since the VA further considers the relationship between the frequency points at adjacent time points based on the maximum value search, it can perform well in the IF extraction.

According to (13), the IF estimation problem can be equivalently considered as the optimal path selection problem on the discrete TF representation. The VA-based IF extraction process is composed of the following steps.

1) Initialization Steps: Initialization Processing:

a) Initialization step one: time–frequency analysis of the received signal: The STFT is performed on the received signal, and the TF representation $\text{STFT}(m,\omega)$ that indicates the relationship between TF can be obtained.

b) Initialization step two: penalty function construction: The TF representation $\text{STFT}(m,\omega)$ is arranged in the nonincreasing order to construct the nonincreasing penalty function $\vartheta(x)$ in (12), and the nondecreasing penalty function $\chi(x,y)$ is also defined in (12).

c) Initialization step three: partial optimal path selection at the time m_2: The rth frequency point at the time m_2 is denoted as $\omega_{m_2}^r$, $r = 1, 2, \ldots, R$, and R is the number of frequency points at time m_2. The partial optimal path of each frequency point $\omega_{m_2}^r$ at the time m_2 should be found out and recorded. Specifically for each frequency point $\omega_{m_2}^r$, we add $\chi(x,y)$ and $\vartheta(x)$ to calculate their sum between time m_2 and previous time m_1, and the paths with the minimum values of the sum are recorded as the partial optimal paths at the time m_2. The above requirements are satisfied by the following equations (14) to (16):

$$\gamma\left(g\left(\omega_{m_1}^i|\omega_{m_2}^r\right)|\omega_{m_2}^r\right) = \begin{cases} 100\%, g\left(\omega_{m_1}^i|\omega_{m_2}^r\right) = g\left(\omega_{m_1}^*|\omega_{m_2}^r\right) \\ 0, g\left(\omega_{m_1}^i|\omega_{m_2}^r\right) \ne g\left(\omega_{m_1}^*|\omega_{m_2}^r\right) \end{cases} \tag{14}$$

where $g(\omega_{m_1}^i|\omega_{m_2}^r)$ represents the path from the frequency point $\omega_{m_2}^r$ to the frequency point $\omega_{m_1}^i$, $i = 1, 2, \ldots, R$, and

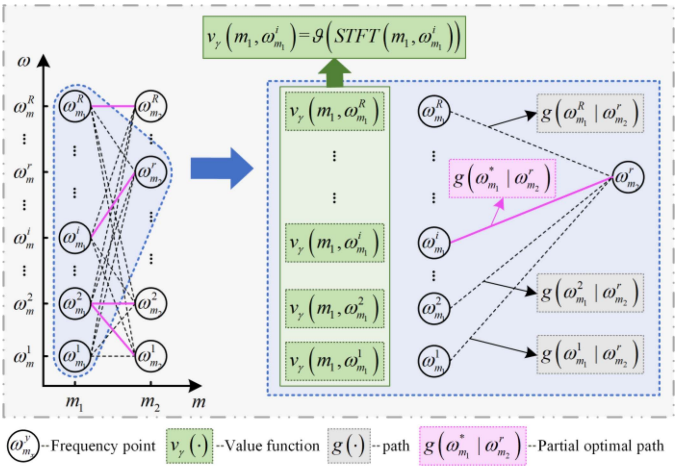

Fig. 3. Diagram for the partial path selection at the time m_2.

R is the number of possible frequency points at time m_1. For the frequency point $\omega_{m_2}^r$, the policy probability function $\gamma(g(\omega_{m_1}^i|\omega_{m_2}^r)|\omega_{m_2}^r)$ in (14) is formulated to select the partial optimal path with 100% probability, which is a deterministic greedy policy with no randomness. The partial optimal path $g(\omega_{m_1}^*|\omega_{m_2}^r)$ for the frequency point $\omega_{m_2}^r$ is described as

$$g\left(\omega_{m_1}^*|\omega_{m_2}^r\right) = \underset{\left\{g\left(\omega_{m_1}^i|\omega_{m_2}^r\right)\right\}_{i=1}^R}{\arg\min} \left\{q\left(\omega_{m_2}^r, g\left(\omega_{m_1}^i|\omega_{m_2}^r\right)\right)\right\} \tag{15}$$

which indicates that the partial optimal path $g(\omega_{m_1}^*|\omega_{m_2}^r)$ can be found by minimizing the combined penalty function $q(\omega_{m_2}^r, g(\omega_{m_1}^i|\omega_{m_2}^r))$, denoted as

$$q\left(\omega_{m_2}^r, g\left(\omega_{m_1}^i|\omega_{m_2}^r\right)\right) = \chi\left(\omega_{m_1}^i, \omega_{m_2}^r\right) + v_\gamma\left(m_1, \omega_{m_1}^i\right) \tag{16}$$

where $v_\gamma(m_1, \omega_{m_1}^i) = \vartheta(\text{STFT}(m_1, \omega_{m_1}^i))$.

The formulated $q(\omega_{m_2}^r, g(\omega_{m_1}^i|\omega_{m_2}^r))$ combines the first penalty function $\vartheta(\text{STFT}(m_1, \omega_{m_1}^i))$ for reaching the frequency point $\omega_{m_1}^i$ [as the first formula in (12)] and the second penalty function $\chi(\omega_{m_1}^i, \omega_{m_2}^r)$ corresponding to the path $g(\omega_{m_1}^i|\omega_{m_2}^r)$ [as the second formula in (12)]. This combined penalty function is acquired when moving from the frequency point $\omega_{m_2}^r$ to the frequency point $\omega_{m_1}^i$ by selecting the path $g(\omega_{m_1}^i|\omega_{m_2}^r)$. The first penalty function $\vartheta(\text{STFT}(m_1, \omega_{m_1}^i))$ is represented by the value function $v_\gamma(m_1, \omega_{m_1}^i)$ for the purpose of consistency with the following iteration steps.

Fig. 3 shows the diagram for the partial path selection at the time m_2. The left half of Fig. 3 represents the partial optimal path $g(\omega_{m_1}^*|\omega_{m_2}^r)|_{r=1,2,\ldots,R}$ selection of each frequency point $\omega_{m_2}^r|_{r=1,2,\ldots,R}$ at the time m_2. The black dotted line shows all of the possible path from the frequency point $\omega_{m_2}^r|_{r=1,2,\ldots,R}$ to its previous time. For each frequency point $\omega_{m_2}^r|_{r=1,2,\ldots,R}$ at the time m_2, the corresponding partial optimal path $g(\omega_{m_1}^*|\omega_{m_2}^r)|_{r=1,2,\ldots,R}$ can be found, which is highlighted with a solid pink line.

Additionally, the detailed instruction for a certain frequency point $\omega_{m_2}^r$ at the time m_2 is shown in the right half of Fig. 3. At the time m_1, the value function $v_\gamma(m_1, \omega_{m_1}^i)|_{i=1,2,\ldots,R}$ can be indicated as the form of the penalty function $\vartheta(\text{STFT}(m_1, \omega_{m_1}^i))|_{i=1,2,\ldots,R}$, as represented in green. On basis of the penalty function $\vartheta(\text{STFT}(m_1, \omega_{m_1}^i))$ and $\chi(\omega_{m_1}^i, \omega_{m_2}^r)$, the partial optimal path $g(\omega_{m_1}^*|\omega_{m_2}^r)$ in (15) can be acquired by minimizing the combined penalty function $q(\omega_{m_2}^r, g(\omega_{m_1}^i|\omega_{m_2}^r))$ in (16). Then, the partial optimal path of a certain frequency point $\omega_{m_2}^r$ at the time m_2 is acquired, indicated as a solid pink line. Moreover, the meanings of the different formulations are shown at the bottom of Fig. 3.

After the three initialization steps mentioned above, the following two iteration steps are proposed to find the partial optimal paths for the other time after the time m_2. For example, in the time $m_l, l \geq 3$, the corresponding partial optimal path $g(\omega_{m_{l-1}}^*|\omega_{m_l}^r)$ can be found by sequentially performing the following two iteration steps, obtained by Fig. 4. The left half of the diagram briefly shows the total iteration process, while the right half describes the two iteration steps in detail, that is, the value function update and the policy function update.

2) Iteration Steps: Partial Optimal Path Selection:

a) Iteration step one: value function update: In the time m_l, the combined penalty function $q(\omega_{m_{l-1}}^r, g(\omega_{m_{l-2}}^i|\omega_{m_{l-1}}^r))$ and the policy function $\gamma(g(\omega_{m_{l-2}}^i|\omega_{m_{l-1}}^r)|\omega_{m_{l-1}}^r)$ for the frequency point $\omega_{m_{l-1}}^r$ at the previous time m_{l-1} are already acquired. Based on the above two functions, the value function of the frequency point $\omega_{m_{l-1}}^r$ can be updated by

$$\begin{aligned} v_\gamma\left(m_{l-1}, \omega_{m_{l-1}}^r\right) &= \vartheta\left(\text{STFT}\left(m_{l-1}, \omega_{m_{l-1}}^r\right)\right) \\ &+ \sum_{\left\{g\left(\omega_{m_{l-2}}^i|\omega_{m_{l-1}}^r\right)\right\}_{i=1}^R} \left\{\gamma\left(g\left(\omega_{m_{l-2}}^i|\omega_{m_{l-1}}^r\right)|\omega_{m_{l-1}}^r\right)\right. \\ &\times \left. q\left(\omega_{m_{l-1}}^r, g\left(\omega_{m_{l-2}}^i|\omega_{m_{l-1}}^r\right)\right)\right\}. \end{aligned} \tag{17}$$

The calculation process of (17) in the value function update step is formally described by the middle part of Fig. 4. Additionally, take $l = 3$ as an example, for the frequency point $\omega_{m_2}^r$, $r = 1, 2, \ldots, R$, its value function $v_\gamma(m_2, \omega_{m_2}^r)$can be computed by (17) based on the policy function $\gamma(g(\omega_{m_1}^i|\omega_{m_2}^r)|\omega_{m_2}^r)$ in (14) and the combined penalty function $q(\omega_{m_2}^r, g(\omega_{m_1}^i|\omega_{m_2}^r))$ in (16).

b) Iteration step two: policy function update: Based on the updated value function $v_\gamma(m_{l-1}, \omega_{m_{l-1}}^r)$, the partial optimal path $g(\omega_{m_{l-1}}^*|\omega_{m_l}^r)$ for the frequency point $\omega_{m_l}^r$ at time m_l can be found by

$$\begin{aligned} &\gamma\left(g\left(\omega_{m_{l-1}}^i|\omega_{m_l}^r\right)|\omega_{m_l}^r\right) \\ &= \begin{cases} 100\%, g\left(\omega_{m_{l-1}}^i|\omega_{m_l}^r\right) = g\left(\omega_{m_{l-1}}^*|\omega_{m_l}^r\right) \\ 0, g\left(\omega_{m_{l-1}}^i|\omega_{m_l}^r\right) \neq g\left(\omega_{m_{l-1}}^*|\omega_{m_l}^r\right) \end{cases} \end{aligned} \tag{18}$$

where $r = 1, 2, \ldots, R$, R is the number of frequency points at time m_l, and $g(\omega_{m_{l-1}}^*|\omega_{m_l}^r)$ is the partial optimal path denoted as

$$g\left(\omega_{m_{l-1}}^*|\omega_{m_l}^r\right) = \underset{\left\{g\left(\omega_{m_{l-1}}^i|\omega_l^r\right)\right\}_{i=1}^R}{\arg\min} \left\{q\left(\omega_{m_l}^r, g\left(\omega_{m_{l-1}}^i|\omega_{m_l}^r\right)\right)\right\} \tag{19}$$

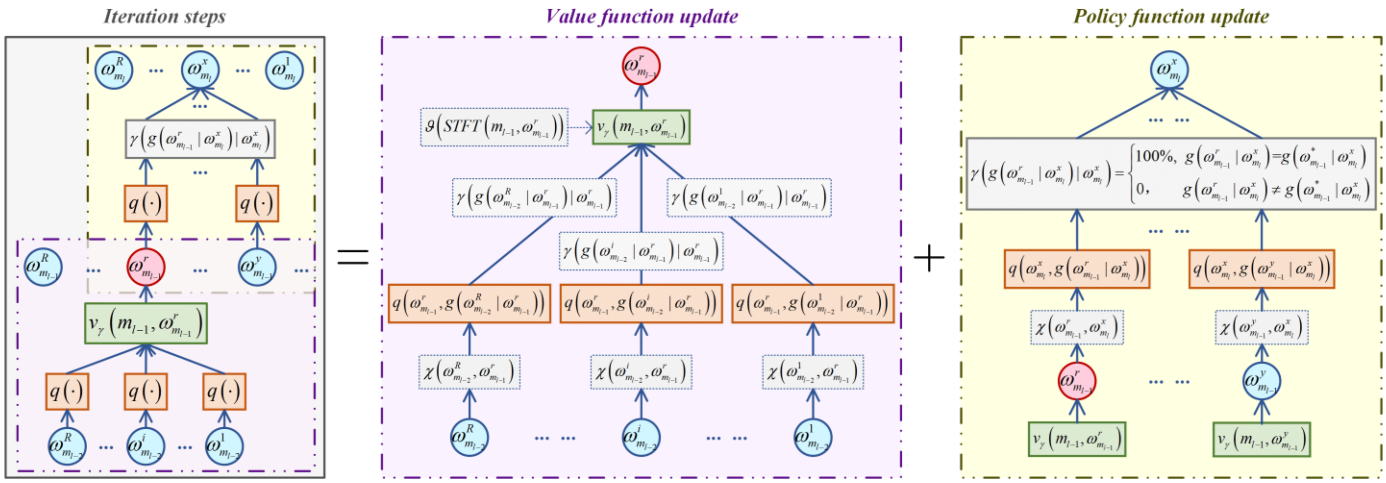

Fig. 4. Diagram of the two iteration steps.

where $q(\omega_{m_l}^r, g(\omega_{m_{l-1}}^i|\omega_{m_l}^r))$ is the combined penalty function obtained when moving from $\omega_{m_l}^r$ to $\omega_{m_{l-1}}^i$ by selecting path $g(\omega_{m_{l-1}}^i|\omega_{m_l}^r)$, described by

$$q\left(\omega_{m_l}^r, g\left(\omega_{m_{l-1}}^i|\omega_{m_l}^r\right)\right) = \chi\left(\omega_{m_{l-1}}^i, \omega_{m_l}^r\right) + v_\gamma\left(m_{l-1}, \omega_{m_{l-1}}^i\right). \tag{20}$$

The calculation process of (18) to (20) in the policy update step is formally described by the right part of Fig. 4. Additionally, take $l = 3$ as an example, for the frequency point $\omega_{m_3}^r$, its partial optimal path $g(\omega_{m_2}^*|\omega_{m_3}^r)$ can be found by computing $q(\omega_{m_3}^r, g(\omega_{m_2}^i|\omega_{m_3}^r))$ based on the penalty function$\chi(\omega_{m_2}^i, \omega_{m_3}^r)$ corresponding to the path $g(\omega_{m_2}^i|\omega_{m_3}^r)$ and the value function $v_\gamma(m_2, \omega_{m_2}^i)$ in (17).

Note that the equations in (14) to (16) are similar to the equations in (17) to (20), the difference is that the value function $v_\gamma(m_1, \omega_{m_1}^i)$ serves as a value function initialization without considering its partial optimal path selection in our realization.

3) Termination Steps: Final Optimal Path Determination:

a) Termination step one: optimal frequency point selection at the time m_L: By analogy, the two iteration steps perform repeatedly at each time point until reaching the time m_L. At the time m_L, the penalty function $\vartheta(x)$ at the time m_L should be considered extra. Therefore, the combined penalty function $q(\omega_{m_L}^r, g(\omega_{m_{L-1}}^i|\omega_{m_L}^r))$ at the time m_L can be written as

$$\begin{aligned} q\left(\omega_{m_L}^r, g\left(\omega_{m_{L-1}}^i|\omega_{m_L}^r\right)\right) &= \chi\left(\omega_{m_{L-1}}^i, \omega_{m_L}^r\right) \\ &\quad + v_\gamma\left(m_{L-1}, \omega_{m_{L-1}}^i\right) \\ &\quad + v_\gamma\left(m_L, \omega_{m_L}^r\right) \end{aligned} \tag{21}$$

where $v_\gamma(m_L, \omega_{m_L}^r) = \vartheta(\mathrm{STFT}(m_L, \omega_{m_L}^r))$.

Finally, the optimal frequency point $\omega_{m_L}^*$ at the time m_L can be obtained by finding the minimum value from the combined penalty function set in

$$\left\{q\left(\omega_{m_L}^r, g\left(\omega_{m_{L-1}}^*|\omega_{m_L}^r\right)\right), \quad r = 1, 2, \ldots, R\right\} \tag{22}$$

where $q(\omega_{m_L}^r, g(\omega_{m_{L-1}}^*|\omega_{m_L}^r))$ represents the combined penalty function of the partial optimal path $g(\omega_{m_{L-1}}^*|\omega_{m_L}^r)$ at the frequency point $\omega_{m_L}^r$, namely

$$\begin{aligned} &q\left(\omega_{m_L}^r, g\left(\omega_{m_{L-1}}^*|\omega_{m_L}^r\right)\right) \\ &= \sum_{\left\{g\left(\omega_{m_{L-1}}^i|\omega_{m_L}^r\right)\right\}_{i=1}^R} \left\{\gamma\left(g\left(\omega_{m_{L-1}}^i|\omega_{m_L}^r\right)|\omega_{m_L}^r\right) q\left(\omega_{m_L}^r,\right.\right. \\ &\quad \left.\left. g\left(\omega_{m_{L-1}}^i|\omega_{m_L}^r\right)\right)\right\}. \end{aligned} \tag{23}$$

b) Termination step two: final optimal path determination via backward recursion: Based on the optimal frequency point $\omega_{m_L}^*$ obtained above, the final optimal path can be acquired via backward recursion from the partial optimal path $g(\omega_{m_{l-1}}^*|\omega_{m_l}^r)$ acquired above. Finally, the IF estimation result $\hat{\omega}_{\mathrm{est}}(m)$ is obtained in terms of the final optimal path.

The diagram of the backward recursion process is shown in Fig. 5. The distribution of all partial optimal path in the STFT-based TF representation is described by the solid pink lines in Fig. 5. From the time m_2 to the time m_L, each frequency point has only one partial optimal path connected with its previous time. On the basis of the optimal frequency point $\omega_{m_L}^*$, the IF estimation of its previous time m_{L-1} can be found along the partial optimal path corresponding to the optimal frequency point $\omega_{m_L}^*$ represented by the solid red line. Then, by the backward recursion along the direction of the red arrow shown in Fig. 5, we can arrive at the final optimal path, which is highlighted with the bold red line. Additionally, the final IF estimation can be acquired through the frequency point on the final optimal path.

From (11), we can see that the IF of the received signal contains the constant term besides the VE. For further processing, the constant term should be removed. Hence, the Fourier transform is employed for removing the constant term, and the estimation of the constant term is acquired as

$$\hat{\omega}_d = \frac{\mathrm{amp}}{L} \tag{24}$$

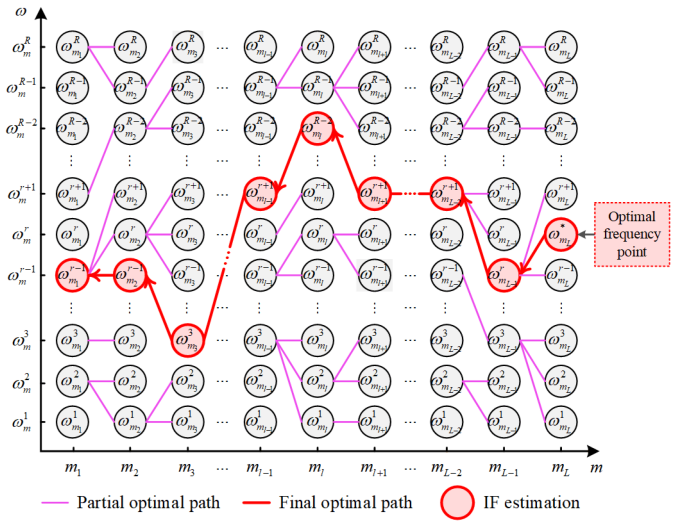

Fig. 5. Diagram of the backward recursion process.

where amp means the amplitude of the zero-frequency component in the Fourier transform result.

After subtracting $\hat{\omega}_d$, the IF including the VE can be represented as

$$\hat{\omega}_{\text{error}}(m) = \hat{\omega}_{\text{est}}(m) - \hat{\omega}_d. \tag{25}$$

The IF $\hat{\omega}_{\text{error}}(m)$ is introduced via the VE, and the parameters need to be estimated for the compensation. Therefore, the RANSAC algorithm with the NLS technique and minimum-entropy principle is used for further processing, which will be discussed next.

B. RANSAC Algorithm Combined With NLS Technique and Minimum-Entropy Principle

In the process of the THz SAR imaging, there may exist noise or platform velocity variation. These factors above lead to the appearance of outliers in the parameter estimation. Moreover, the commonly used parameter estimation method, such as the least square method, uses the distance between all the estimated points and actual points as the criterion. Therefore, the outliers will decrease the estimation precision. Based on the above analysis, the RANSAC algorithm [34] is chosen for the parameter estimation.

The RANSAC algorithm is an iterative algorithm which can correctly estimate the parameters from the data including outliers. For the data to be estimated, it consists of the inliers and the outliers. The former is the data that makes up the model, while the latter does not belong to the model. Moreover, all inliers are determined by a deterministic model.

By repeatedly selecting the data, the RANSAC algorithm iteratively estimates the model until acquiring a satisfying result. Specifically, the NLS technique is introduced for VE estimation in each iteration, whose objective function can be indicated as

$$f\left(\dot{\alpha}_q, \dot{\eta}_q, \dot{\phi}_q\right) = \frac{1}{2}\left\|\hat{\omega}_{\text{error}}(m) - y_{\text{model}}\right\|_2^2 \tag{26}$$

where $\|\|_2$ indicates the two-norm, $q = 1, 2, \ldots, Q$, y_{model} is the VE parameter estimation model, which is superimposed via Q sinusoidal signals. Furthermore, $\dot{\alpha}_q$, $\dot{\eta}_q$, and $\dot{\phi}_q$ represent the qth amplitude, frequency, and initial phase in parameter estimation model y_{model}, respectively. By minimizing $f(\dot{\alpha}_q, \dot{\eta}_q, \dot{\phi}_q)$, we can obtain the vibration parameter estimation result $(\hat{\alpha}_q, \hat{\eta}_q, \hat{\phi}_q)$.

In THz SAR imaging process, the parameter estimation aims to acquire the well-focused imaging results. Therefore, after the iteration in the RANSAC algorithm, we use the minimum-entropy principle to select the optimal solution. The specific implementations of the RANSAC algorithm are decomposed into five steps.

1) Iteration Step One: Initial Fitting Model Construction via K Random Points: First, we select K random points from $\hat{\omega}_{\text{error}}(m)$, and the NLS technique is performed on the K points to acquire the initial fitting model, shown as

$$\omega_{\text{model}} = \text{NLS}\left[\omega_K\right] \tag{27}$$

where ω_{model} means the fitting model, NLS$[\cdot]$ indicates the NLS operation, and ω_K is composed of the K random points from $\hat{\omega}_{\text{error}}(m)$.

2) Iteration Step Two: Inlier Selection: Second, all points in $\hat{\omega}_{\text{error}}(m)$ are tested via the initial model fitted in *Step 1*. As shown in (28), if a point in $\hat{\omega}_{\text{error}}(m)$ fits the initial model, it is denoted as an inlier. Additionally, the other points are indicated as the outliers, denoted as follows:

$$\omega_{\text{inlier}} = \left\{\hat{\omega}_{\text{error}}(m) \,|\hat{\omega}_{\text{error}}(m) \in \omega_{\text{model}}\right\} \tag{28}$$

$$\omega_{\text{outlier}} = \left\{\hat{\omega}_{\text{error}}(m) \,|\hat{\omega}_{\text{error}}(m) \notin \omega_{\text{model}}\right\} \tag{29}$$

where ω_{inlier} and ω_{outlier} are the inliers and outliers, respectively.

3) Iteration Step Three: Fitting Model Update: Third, all inliers are refitted via the NLS technique, and the fitting model is updated, expressed as follows:

$$\omega_{\text{model}} = \text{NLS}\left[\omega_{\text{inlier}}\right]. \tag{30}$$

4) Iteration Step Four: Image Entropy Computation: Fourth, the updated fitting model is used to construct the compensation function. After the compensation, the image entropy defined as follows is calculated, which is used as the judgment criterion:

$$E = -\sum_{\rho=1}^{\text{P}}\sum_{\nu=1}^{\Upsilon}\left[\frac{|s(\rho,\nu)|^2}{\sum_{\rho=1}^{\text{P}}\sum_{\nu=1}^{\Upsilon}|s(\rho,\nu)|^2} \times \ln\left(\frac{|s(\rho,\nu)|^2}{\sum_{\rho=1}^{\text{P}}\sum_{\nu=1}^{\Upsilon}|s(\rho,\nu)|^2}\right)\right] \tag{31}$$

where $|s(\rho,\nu)|$ represents the discrete image.

5) Termination Step: Best Fitting Model Selection: Finally, the iteration from *Step 1* to *Step 4* continues until the maximum number of the iteration is met, and the minimum-entropy principle is employed to choose the best model, as denoted in (32). The final parameter estimation result is obtained via the model that minimizes the image entropy.

$$\left(\hat{\alpha}_q, \hat{\eta}_q, \hat{\phi}_q\right)_{\text{best}} = \underset{\left(\hat{\alpha}_q, \hat{\eta}_q, \hat{\phi}_q\right)}{\text{argmin}}\left\{E_{\text{RANSAC}}\right\} \tag{32}$$

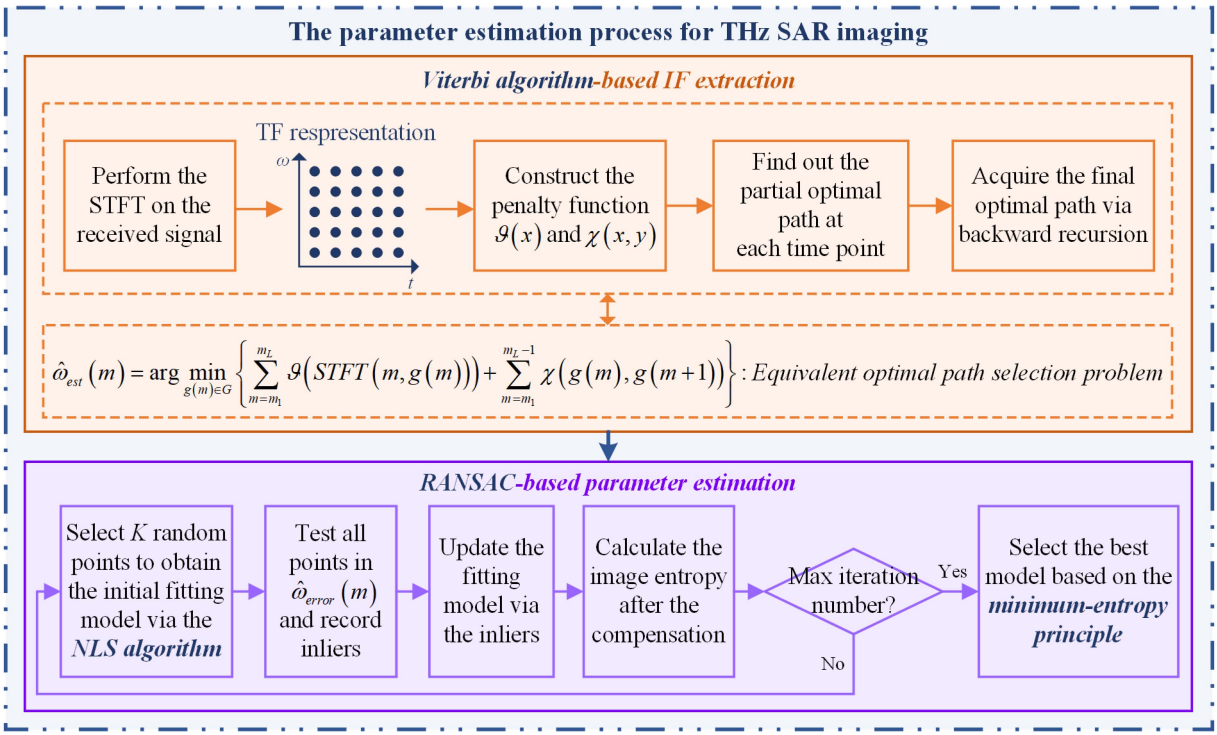

Fig. 6. Flow chart of the parameter estimation process for THz SAR imaging.

where E_{RANSAC} denotes the image entropy set that calculates using the updated fitting models in RANSAC iterations, and $(\hat{\alpha}_q,\hat{\eta}_q,\hat{\phi}_q)_{\mathrm{best}}$ means the best parameter estimation result selection.

Each iteration (that is, *Step 1* to *Step 4*) produces a fitting model with two outcomes. One is that the model is discarded since the image entropy obtained via the model is higher than that of the last iteration, and the other is that the model is selected because it is better than the existing models. Through the iterations, the RANSAC algorithm can exclude the interference factors, such as the noise or the platform velocity variation, and select the inliers belonging to the high-frequency VE for parameter estimation, which improves the accuracy of parameter estimation.

After the parameter estimation via the VA and the RANSAC algorithm, the VE compensation is finished by compensation function construction, and the azimuth image defocus is inhibited. Moreover, the flow chart of the parameter estimation process for the THz SAR imaging is shown in Fig. 6.

IV. Experimental Results

A. Simulation Experiment Results

Through the proposed method in this article, the simulation experiments for the VE compensation at different signal-to-noise ratios (SNRs) will be discussed as follows.

1) Case 1: The Simulation Experiment for VE Compensation Under 10 dB SNR: In the simulation experiment, the echo signal of the THz SAR system is modeled by setting eight identical scattering points in the imaging scenario, and their reflection coefficients are set to the same value, which is shown in Fig. 7. Moreover, the corresponding simulation parameters are shown in Table I.

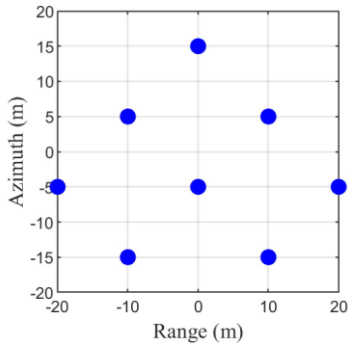

Fig. 7. Scatter point model in the imaging scene.

TABLE I
Summary of Simulation Parameters

Parameter	Value	Parameter	Value
Carrier frequency	220 GHz	PRF	2500 Hz
Bandwidth	4 GHz	Sampling rate	4.8 GHz
Pulse width	1 μs	Synthetic aperture time	0.4724 s
Platform height	3000 m	Range resolution	3.75 cm
Platform speed	100 m/s	Azimuth resolution	5 cm

In this case, the echo signal with the platform high-frequency VE is modeled under 10 dB SNR, which is defined in the data

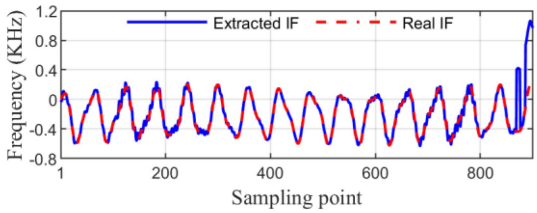

Fig. 8. IF extracted via the TF ridge under 10 dB SNR.

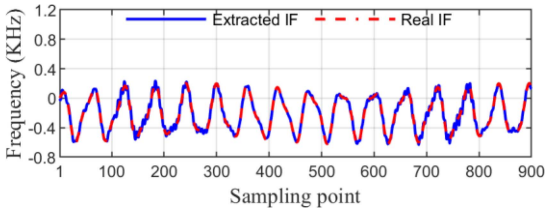

Fig. 9. IF extracted via the VA under 10 dB SNR.

TABLE II
NRMSE BETWEEN THE EXTRACTED IF AND THE REAL IF UNDER 10 DB SNR

Methods	TF ridge	VA
NRMSE	0.4243	0.0866

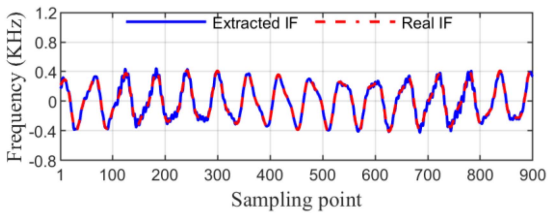

Fig. 10. IF extracted via the VA after removing the constant term under 10 dB SNR.

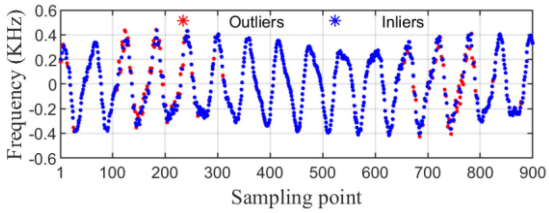

Fig. 11. Inliers and outliers acquired via the RANSAC method under 10 dB SNR.

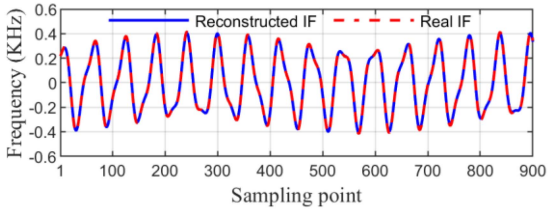

Fig. 12. Reconstructed IF via our proposed method under 10 dB SNR.

after the range compression. To compensate the VE and obtain the focused images, the IF of the echo signal should be extracted at first, and its extraction accuracy directly affects the accuracy of the subsequent VE compensation. Therefore, we use the TF ridge extraction algorithm for comparison to prove the superiority of our proposed algorithm in IF extraction. The IFs extracted via the STFT-based TF ridge and the VA are displayed in Figs. 8 and 9, respectively. From Fig. 8, we can see that in multipoint target imaging scenarios lacking isolated strong scattering point, the IF extracted via the TF ridge exhibits some relatively noticeable errors compared to the real values under 10 dB SNR. However, the VA can avoid this problem to some extent, and extract the IF with high precision.

Compared with the TF ridge extraction algorithm which directly searches for the maximum value from the frequency points corresponding to each time point, the VA algorithm further considers the relationship between frequency points at adjacent time points based on the maximum value search, which are also the hypotheses that VA needs to satisfy. Since the VA is defined based on the characteristics of the IF, it can accurately extract IF in multipoint target imaging scenarios lacking isolated strong scattering point. Through choosing the appropriate values of c and Δ, the VA can select the optimal path between the frequency points at adjacent time points. Then, the IF containing the VE information is extracted from the TF representation via the VA for the subsequent VE compensation.

In order to further prove the superiority of the proposed algorithm numerically, the normalized root mean square error (NRMSE) is introduced to measure the error between the extracted IF and the real IF, as shown in Table II. Obviously, the smaller NRMSE further proves numerically that our proposed algorithm has higher accuracy than the TF ridge extraction in the IF extraction.

The Fourier transform is then performed on the extracted IF, and the constant term is removed. The significance of removing the constant component is to remove the direct current component from the IF signal, retaining the alternating current component containing the VE information, thereby preparing for the subsequent parameter estimation. After subtracting the constant term, the IF acquired via the VA is shown in Fig. 10. Then, we further estimate the VE through the RANSAC algorithm. Additionally, the NLS technique is performed on K random points of the extracted IF to estimate the parameters in each iteration, and the minimum-entropy principle is used for the best model selection. The inliers and the outliers that the RANSAC algorithm chooses are shown in Fig. 11. It is clear that the RANSAC algorithm excludes the outliers introduced by the noise, besides, it selects the points that are suitable for the model from $\hat{\omega}_{\text{error}}(m)$ as the inliers for the parameter estimation. The parameter estimation using the inliers will reduce the interference of the noise, and obtain the higher precision. The reconstructed IF after the parameter estimation via our proposed method is displayed in Fig. 12.

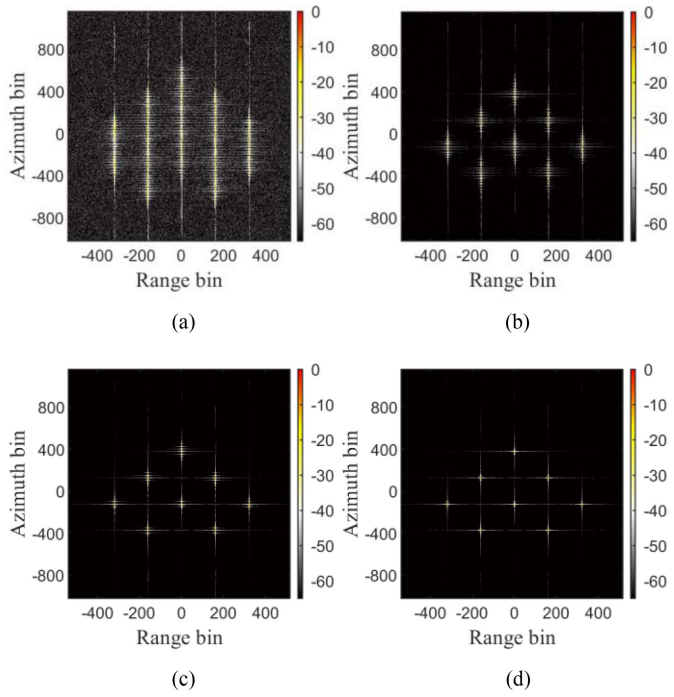

Fig. 13. SAR images acquired via the proposed method and the other two comparison methods under 10 dB SNR. (a) SAR image without the VE compensation. (b) SAR image acquired via the PSP-based method. (c) SAR image acquired via the NLS-based method. (d) SAR image acquired via our method.

In this article, we use two algorithms for comparison. The first comparison method combines the STFT with the parameter space projection (PSP). As for the PSP-based method, the STFT is used for the TF ridge extraction to estimate the vibration frequency via the Fourier transform, and the PSP is then used for the estimation of the vibration amplitude and the vibration initial phase. Another comparison method is based on the STFT and the NLS technique. In the NLS-based method, the NLS technique is used to estimate the parameters of the STFT-based TF ridge, then the VE parameters can be estimated. The two comparison methods aim to illustrate the superiority of the VA and the RANSAC algorithm combined with the NLS technique and the minimum-entropy principle. Compared with the STFT-based TF ridge extraction, the VA-based IF extraction has better performance. Furthermore, compared with the direct parameter estimation via the NLS technique, we combine the RANSAC algorithm with the NLS technique and the minimum-entropy principle in this article, which can obtain the more accurate parameter estimation results and the better antinoise performance. The parameter estimation results via different methods are displayed in Table III. From the parameter estimation results in Table III, it can be seen that our proposed method can obtain the accurate estimation results, and it has better estimation performance than the other two methods.

After the vibration parameter estimation, the compensation function is constructed, and the VE can be compensated. Fig. 13 provides the corresponding imaging results about the VE compensation. Fig. 13(a) displays the SAR image without the VE

TABLE III
PARAMETER ESTIMATION RESULTS VIA DIFFERENT METHODS UNDER 10 DB SNR

Parameters		Methods	Real values	Estimated values	Absolute error
Vibration amplitude	a_1 (mm)	PSP	0.8267	0.7813	0.0454
		NLS		0.8474	0.0207
		Proposed method		0.8171	0.0096
	a_2 (mm)	PSP	0.1181	0.2387	0.1206
		NLS		0.1347	0.0166
		Proposed method		0.1105	0.0076
Vibration frequency	f_1 (Hz)	PSP	42	42.1389	0.1389
		NLS		42.0975	0.0975
		Proposed method		41.9973	0.0027
	f_2 (Hz)	PSP	88	87.9444	0.0556
		NLS		87.9682	0.0318
		Proposed method		88.0334	0.0334
Vibration initial phase	φ_1 (rad)	PSP	0.5585	0.4538	0.1047
		NLS		0.6324	0.0739
		Proposed method		0.5558	0.0027
	φ_2 (rad)	PSP	1.1868	1.2915	0.1047
		NLS		1.1608	0.0260
		Proposed method		1.2125	0.0257

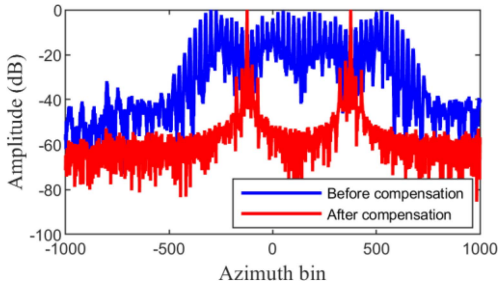

Fig. 14. Profiles along the azimuth direction processed by our proposed method under 10 dB SNR.

compensation, and it is seriously defocused along the azimuth direction, which can be suppressed through the following VE compensation. The imaging results after the PSP-based method and the NLS-based method are, respectively, shown in Fig. 13(b) and (c), which are still defocused along the azimuth direction. Furthermore, as shown in Fig. 13(d), the scattering points are clear to be distinguished by using the proposed method. Hence, the proposed method performs better in IF extraction and parameter estimation of the THz SAR VE compensation under 10 dB SNR.

Additionally, the image entropy of the SAR images above is provided in Table IV for the further comparison. Obviously,

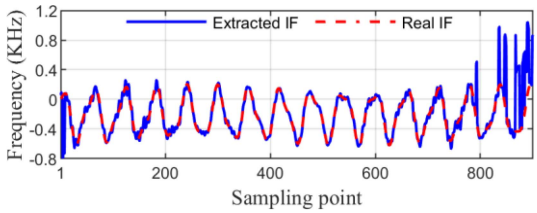

Fig. 15. IF extracted via the TF ridge under 0 dB SNR.

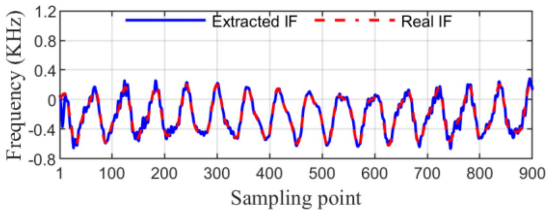

Fig. 16. IF extracted via the VA under 0 dB SNR.

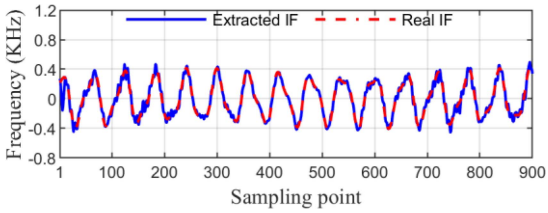

Fig. 17. IF extracted via the VA after removing the constant term under 0 dB SNR.

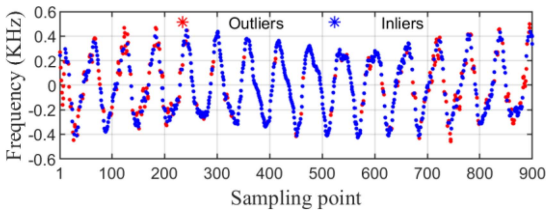

Fig. 18. Inliers and outliers acquired via the RANSAC method under 0 dB SNR.

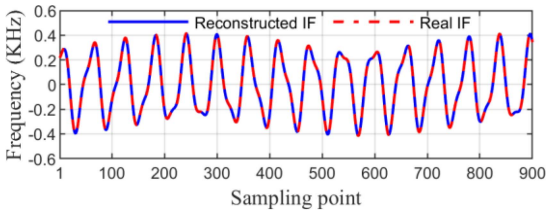

Fig. 19. Reconstructed IF via our proposed method under 0 dB SNR.

TABLE IV
IMAGE ENTROPY OBTAINED VIA DIFFERENT METHODS UNDER 10 DB SNR

Figs	Fig. 13 (a)	Fig. 13 (b)	Fig. 13 (c)	Fig. 13 (d)
Image entropy	9.1627	7.6775	6.3184	5.4174

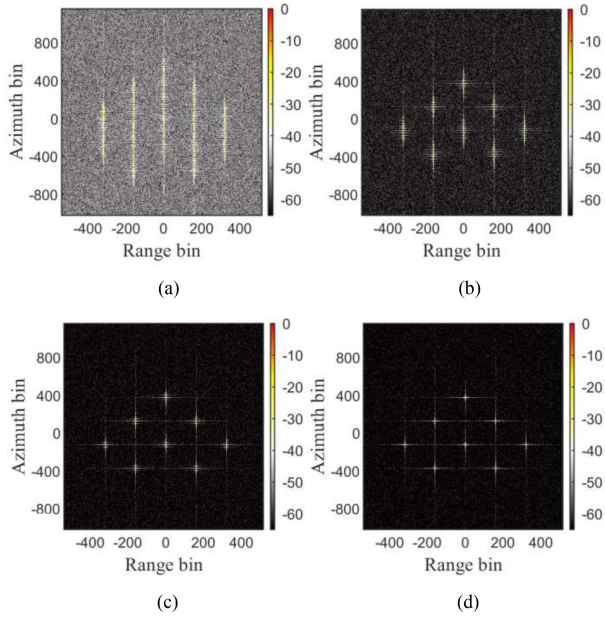

Fig. 20. SAR images acquired via the proposed method and the other two comparison methods under 0 dB SNR. (a) SAR image without the VE compensation. (b) SAR image acquired via the PSP-based method. (c) SAR image acquired via the NLS-based method. (d) SAR image acquired via our method.

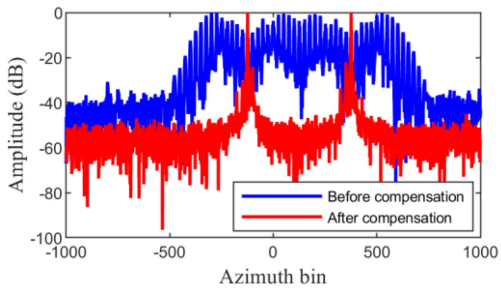

Fig. 21. Profiles along the azimuth direction processed by our proposed method under 0 dB SNR.

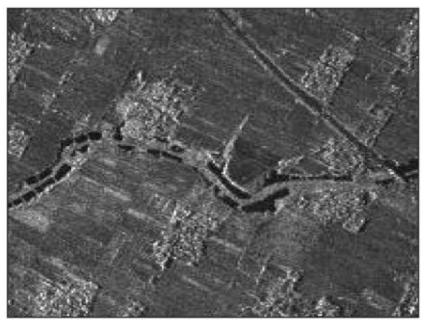

Fig. 22. X-band SAR imaging results of the real ground scene.

the performance of the proposed method in this article is surpassed by the other two comparison methods. Finally, Fig. 14 displays the profiles along the azimuth direction processed by our method, where the defocus caused by VE is significantly inhibited.

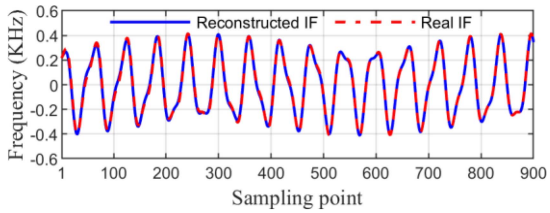

Fig. 23. Reconstructed IF via our proposed algorithm in the semiphysical simulation experiment.

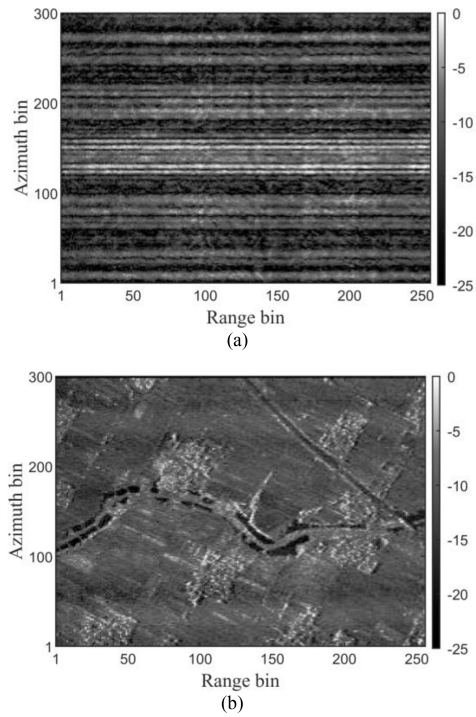

Fig. 24. SAR images acquired via the proposed method in the semiphysical simulation experiment. (a) SAR image without the VE compensation. (b) SAR image acquired via our method.

Fig. 25. Scenario description of the imaging experiment.

2) Case 2: The Simulation Experiment for VE Compensation Under 0 dB SNR: In this case, in order to further investigate the performance of the VA and the RANSAC algorithm, we conduct the simulation experiment for VE compensation under 0 dB SNR using the scatter point model in Fig. 7 and the simulation parameters in Table I, and the SNR is defined in the data after the range compression. Similarly, the IFs extracted via the STFT-based TF ridge and the VA are shown in Figs. 15 and 16, respectively. It is obvious that there exist some relatively noticeable errors in the IF extracted via the TF ridge compared to the real value in Fig. 15. Additionally, the NRMSE between the extracted IF and the real IF is shown in Table V. The smaller NRMSE in Table V proves that the VA algorithm can extract the IF more accurately. Therefore, compared with the TF ridge-based IF extraction, the VA has a better performance of the IF extraction in multipoint target imaging scenarios lacking isolated strong scattering point under 0 dB SNR.

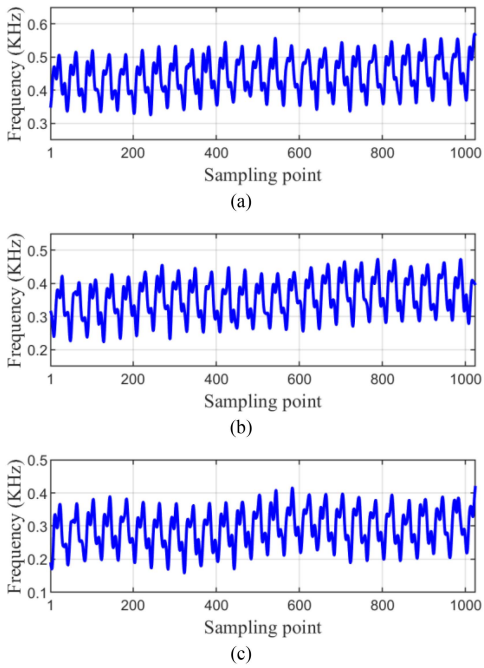

Fig. 26. Result of IF extraction by the VA. (a) Extracted IF in the digit 8 case. (b) Extracted IF in the digit 6 case. (c) Extracted IF in the digit 3 case.

TABLE V
NRMSE BETWEEN THE EXTRACTED IF AND THE REAL IF UNDER 0 DB SNR

Methods	TF ridge	VA
NRMSE	0.5255	0.1441

Then, after removing the constant term via the Fourier transform, the IF extracted via the VA is shown in Fig. 17. Based on the extracted IF in Fig. 17, the RANSAC algorithm is employed for further process. In each iteration, the NLS technique is used to fit the K randomly selected points in the extracted IF, and the minimum-entropy principle is finally used to choose the best model in all iteration results. The inliers and the outliers acquired via the RANSAC algorithm are shown in Fig. 18. Obviously, the RANSAC algorithm can mitigate the interference of the errors introduced via the noise and the IF extraction from the previous step. Due to the presence of higher noise, the RANSAC algorithm excludes more outliers at the SNR of 0 dB than at the SNR of 10 dB. Through getting rid of these outliers, the precise parameter estimation results can be obtained by using the inliers for the parameter estimation, which is shown in Fig. 19.

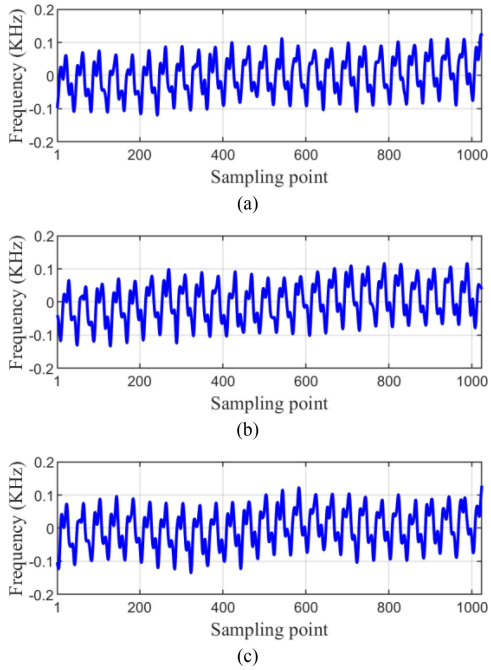

Fig. 27. Result of IF extraction by the VA after removing the constant term. (a) IF extracted via the VA after removing the constant term in the digit 8 case. (b) IF extracted via the VA after removing the constant term in the digit 6 case. (c) IF extracted via the VA after removing the constant term in the digit 3 case.

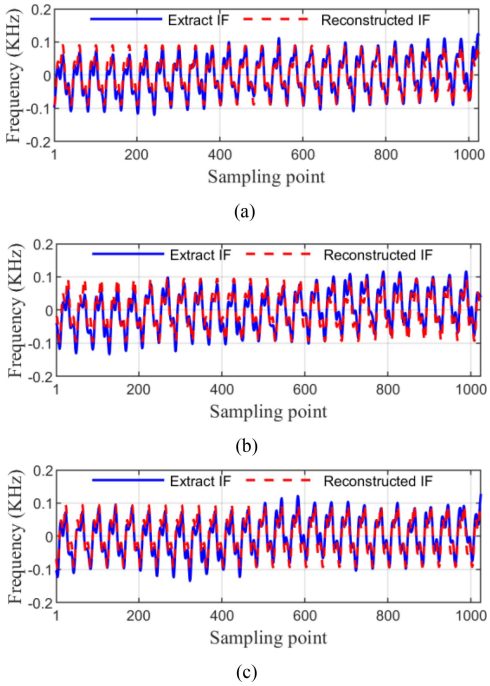

Fig. 29. IF reconstruction via our proposed method. (a) Reconstructed IF by our proposed method in the digit 8 case. (b) Reconstructed IF by our proposed method in the digit 6 case. (c) Reconstructed IF by our proposed method in the digit 3 case.

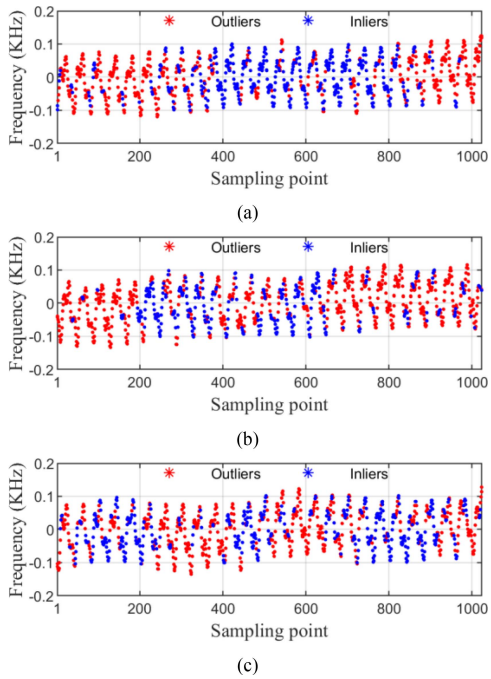

Fig. 28. Both the inliers and outliers acquired by RANSAC. (a) Inliers and the outliers acquired via the RANSAC algorithm in the digit 8 case. (b) Inliers and the outliers acquired via the RANSAC algorithm in the digit 6 case. (c) Inliers and the outliers acquired via the RANSAC algorithm in the digit 3 case.

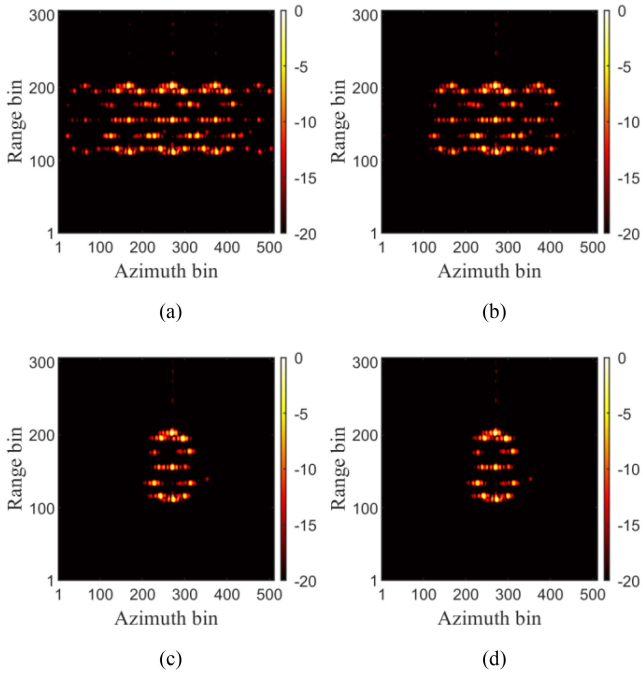

Fig. 30. Imaging results acquired via the proposed method and the other two compensation methods in the digit 8 case. (a) SAR image without VE compensation. (b) SAR image acquired via the PSP-based method. (c) SAR image acquired via the NLS-based method. (d) SAR image acquired via our method.

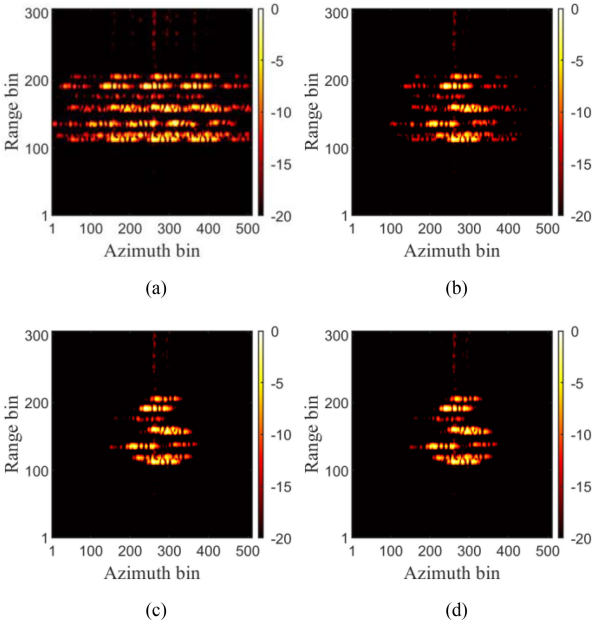

Fig. 31. Imaging results acquired via the proposed method and the other two compensation methods in the digit 6 case. (a) SAR image without VE compensation. (b) SAR image acquired via the PSP-based method. (c) SAR image acquired via the NLS-based method. (d) SAR image acquired via our method.

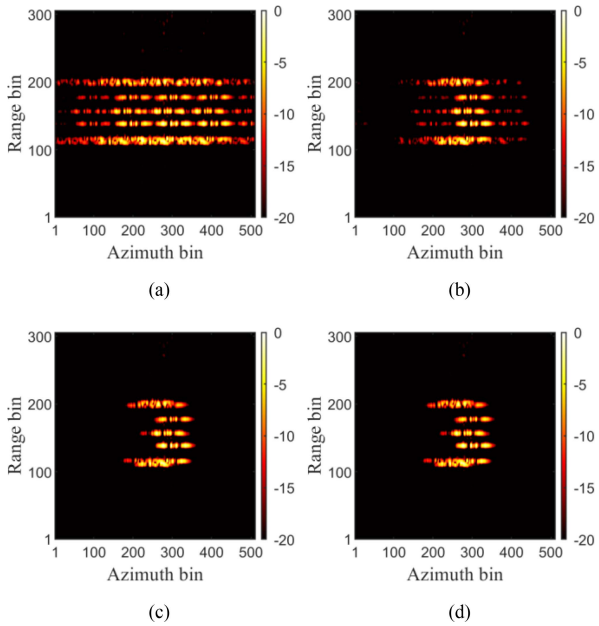

Fig. 32. Imaging results acquired via the proposed method and the other two compensation methods in the digit 3 case. (a) SAR image without VE compensation. (b) SAR image acquired via the PSP-based method. (c) SAR image acquired via the NLS-based method. (d) SAR image acquired via our method.

Homoplastically, the PSP-based method and the NLS-based method are employed for comparison. Table VI summarizes the corresponding vibration parameter estimation results. Compared with the other two methods, the RANSAC algorithm can estimate the parameters with higher precision.

We can further compensate the VE based on the parameter estimation results above. Through different methods, the imaging results after the VE compensation are shown in Fig. 20. Fig. 20(a) shows the imaging result without the compensation. Fig. 20(b) and (c), respectively, describe the SAR images through the PSP-based and the NLS-based compensation methods. Fig. 20(d) corresponds to the SAR image acquired by our method. The defocus is still not completely compensated in the SAR images processed by the two comparison methods. However, by compensating using our proposed method, the scattering points in the imaging results are distinct. The results above demonstrate that our proposed method provides higher precision and better performance even under 0 dB SNR.

Additionally, the image entropy of the SAR images in Fig. 20 is provided in Table VII for further explanation. Compared with the other two compensation methods, our proposed method can provide the best focused SAR image. Finally, Fig. 21 displays the profiles along the azimuth direction acquired via our method. The focusing effect is obviously improved after compensating by our proposed method.

3) Case 3: The Semiphysical Simulation Experiment for VE Compensation: To better align with practical conditions and further validate the effectiveness of the proposed algorithm in complex scenarios, we conducted the semiphysical simulation experiment based on the actual X-band SAR image in Case 3.

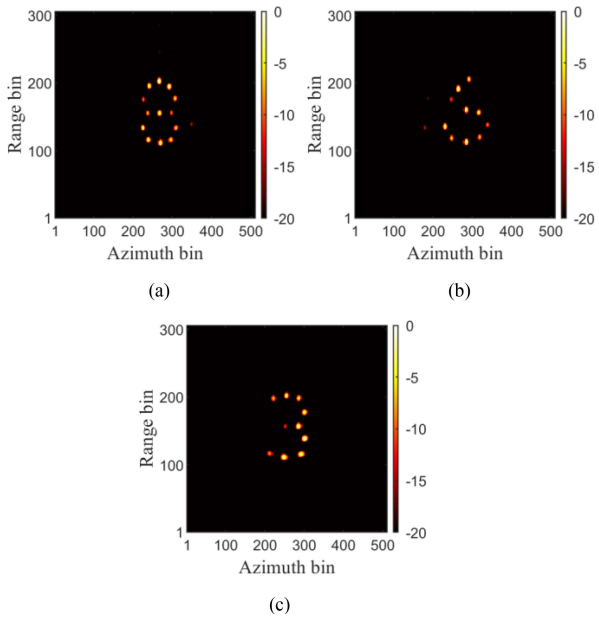

Fig. 33. Final SAR images after compensating VE by our method and the PGA method. (a) Final SAR image in the digit 8 case. (b) Final SAR image in the digit 6 case. (c) Final SAR image in the digit 3 case.

Specifically, the X-band SAR imaging result of the real ground scene is shown in Fig. 22. To reconstruct the scatter points model of the actual ground SAR image in Fig. 22, we establish a corresponding scatter point for each pixel in Fig. 22 within the scatter points model and convert the gray value of each pixel to the amplitude value of the corresponding scatter point. Then, based on this scatter points model, we reconstruct the

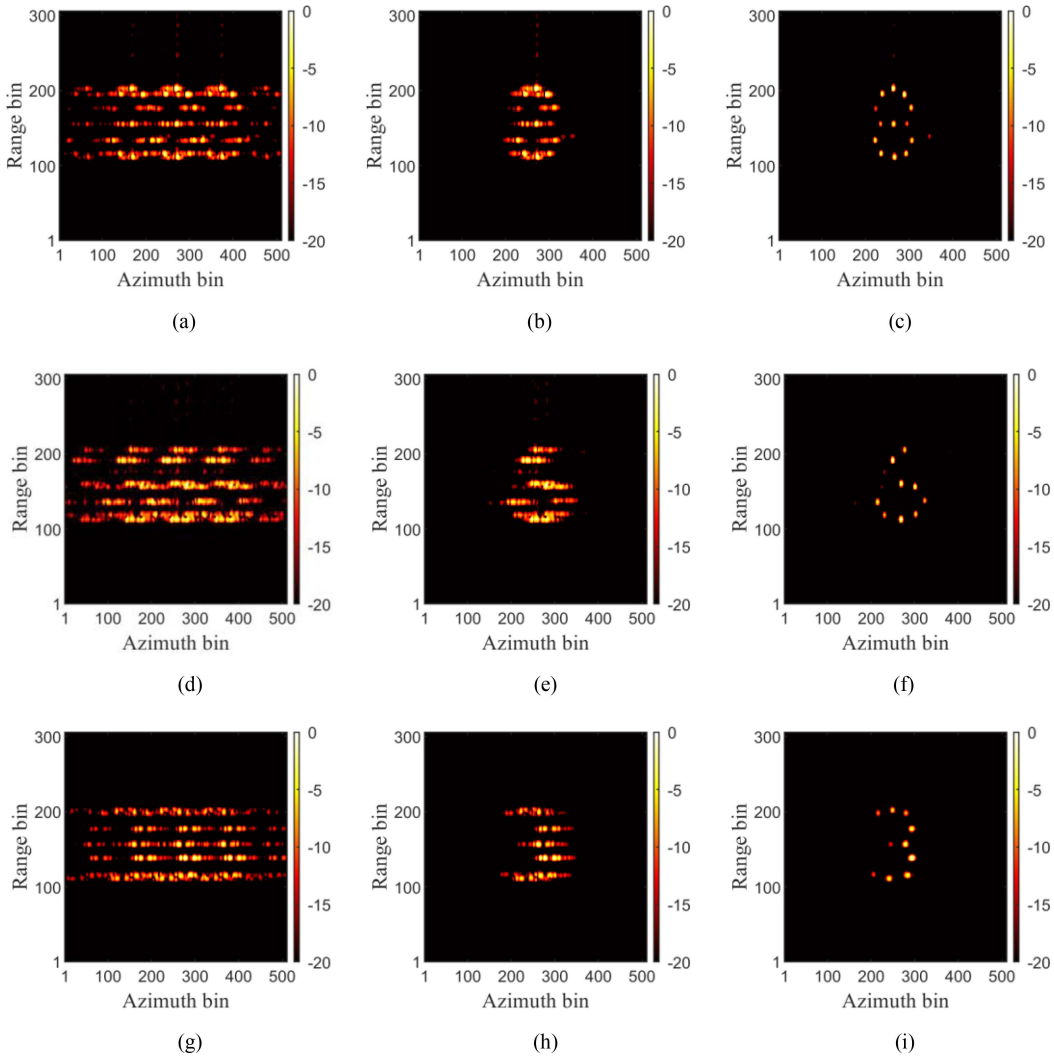

Fig. 34. Imaging results of the additional set of data segments. (a) SAR image without VE compensation in the digit 8 case. (b) SAR image acquired via our method in the digit 8 case. (c) SAR image acquired via our method and the PGA algorithm in the digit 8 case. (d) SAR image without VE compensation in the digit 6 case. (e) SAR image acquired via our method in the digit 6 case. (f) SAR image acquired via our method and the PGA algorithm in the digit 6 case. (g) SAR image without VE compensation in the digit 3 case. (h) SAR image acquired via our method in the digit 3 case. (i) SAR image acquired via our method and the PGA algorithm in the digit 3 case.

echo signal model containing the platform VE in the THz band and apply our proposed algorithm for compensation and imaging.

By using our proposed algorithm, the platform VE parameters can be estimated and the IF can be reconstructed to construct the compensation function, as shown in Fig. 23. Using the compensation function, the phase error caused by platform VE can be removed, and the image defocus along the azimuth direction can be suppressed.

As shown in Fig. 24(a), due to the influence of VE, the THz SAR imaging results without VE compensation are severely defocused along the azimuth direction, leading to significantly blurred SAR images. Fig. 24(b) shows the imaging results obtained after the VE compensation using the proposed algorithm. It can be seen that the defocus caused by the platform VE is suppressed, and the clearly focused THz SAR image of the ground scene is obtained.

Finally, Table VIII shows the entropy of the THz SAR images in Fig. 24 before and after the VE compensation. The reduction in entropy further demonstrates the effectiveness of the proposed algorithm.

B. Real-Measured Experiment Results

In the real-measured experiment, the existence of the platform velocity variation may cause points to deviate from the real IF, leading to the decrease of the parameter estimation accuracy. Therefore, in Section IV-B, the real-measured data are used to further demonstrate the effectiveness of our proposed algorithm under platform speed variation. The bandwidth and the carrier frequency of the real-measured system are 4.8 and 216 GHz, respectively. The radar transmits the signals with the pulse repetition frequency of 2000 Hz. Moreover, with the range resolution of 3.125 cm and the azimuth resolution of 3.2 cm,

TABLE VI
PARAMETER ESTIMATION RESULTS VIA DIFFERENT METHODS UNDER 0 DB SNR

Parameters		Methods	Real Values	Estimated Values	Absolute error
Vibration amplitude	a_1 (mm)	PSP	0.8267	0.7813	0.0454
		NLS		0.8156	0.0111
		Proposed method		0.8229	0.0038
	a_2 (mm)	PSP	0.1181	0.2387	0.1206
		NLS		0.1196	0.0015
		Proposed method		0.1155	0.0026
Vibration frequency	f_1 (Hz)	PSP	42	42.1111	0.1111
		NLS		42.0631	0.0631
		Proposed method		41.9922	0.0078
	f_2 (Hz)	PSP	88	87.9722	0.0278
		NLS		87.9728	0.0272
		Proposed method		87.9931	0.0069
Vibration initial phase	φ_1 (rad)	PSP	0.5585	0.4538	0.1047
		NLS		0.6201	0.0616
		Proposed method		0.5582	0.0003
	φ_2 (rad)	PSP	1.1868	1.2915	0.1047
		NLS		1.0438	0.1430
		Proposed method		1.1677	0.0191

TABLE VII
IMAGE ENTROPY OBTAINED VIA DIFFERENT METHODS UNDER 0 DB SNR

Figs	Fig. 20 (a)	Fig. 20 (b)	Fig. 20 (c)	Fig. 20 (d)
Image entropy	12.9710	11.9007	10.8959	10.5262

TABLE VIII
IMAGE ENTROPY OF FIG. 24

Figs	Fig. 24 (a)	Fig. 24 (b)
Image entropy	12.0903	11.5500

the radar images the scene shown in Fig. 25 on the trolley at the speed of $0.35\mathrm{m/s}$. Additionally, the vertical distance from radar to the scene and the height of the antenna is 4 and $1.2\,\mathrm{m}$, and the synthetic aperture time is 0.26 s.

In the real-measured imaging scene, there exist three digits, that is, digit 8, digit 6, and digit 3. After the systematic amplitude-phase error compensation, the echo data are further processed to compensate the VE based on our proposed method. First, the VA is employed for the IF extraction, which is shown in Fig. 26. Then, the IF above is further processed by the Fourier transform, and the IF after removing the constant term is shown in Fig. 27.

TABLE IX
IMAGE ENTROPY OBTAINED VIA DIFFERENT METHODS

Scenes		Image entropy
Digit 8	Fig. 30 (a)	9.5175
	Fig. 30 (b)	9.2419
	Fig. 30 (c)	8.3098
	Fig. 30 (d)	8.3068
Digit 6	Fig. 31 (a)	9.9938
	Fig. 31 (b)	9.3335
	Fig. 31 (c)	8.9133
	Fig. 31 (d)	8.9114
Digit 3	Fig. 32 (a)	9.8776
	Fig. 32 (b)	9.1942
	Fig. 32 (c)	8.7777
	Fig. 32 (d)	8.7742

In the real-measured system, due to the uneven platform velocity or the platform motion trajectory deviation, there will exist errors caused by platform velocity variation in the IF. The error introduced via the platform velocity variation will affect the subsequent estimation of the platform high-frequency VE. Thus, the RANSAC method is used for further processing to remove the points that do not belong to the high-frequency VE model. Then, the best model is selected based on the minimum-entropy principle after the parameter estimation via the NLS technique in each iteration, and the final inlier and outlier selection via the RANSAC algorithm is shown in Fig. 28. As shown in Fig. 28, only a part of the points, namely, the inliers, are selected for the parameter estimation, and the points that do not belong to the high-frequency vibration model, such as the deviation points caused by the platform velocity variation or the noise, will be removed from the final parameter estimation. Based on the estimated parameters, the reconstructed IF result is shown in Fig. 29.

Based on the reconstructed IF in Fig. 29, the compensation function can be constructed to remove the VE. Similarly, the PSP-based method and the NLS-based method are used for comparison. The SAR image without any compensation in Fig. 30(a) is seriously defocused. In the digit 8 case, the SAR images with the VE compensation by using the two comparison methods and the proposed method are shown in Fig. 30(b)–(d). In the same way, the imaging results of the digit 6 and the digit 3 obtained via different methods are shown in Figs. 31 and 32, respectively.

Additionally, Table IX provides the image entropy of Figs. 30–32 for further comparison. This table demonstrates that our proposed method can acquire the best focused SAR image among the three VE compensation methods.

The SAR images in Figs. 30–32 are still defocused on account of the platform velocity variation. Consequently, the phase grade autofocus (PGA) algorithm is employed for further compensation. Fig. 33 displays the final SAR images after VE compensation through our proposed method and the PGA method. For the SAR images in Fig. 33(a)–(c), the corresponding image entropies are 7.4189, 7.3939, and 7.3876. The SAR images in Fig. 33 are well-focused and its defocus can be inhibited well.

TABLE X
IMAGE ENTROPY OF FIG. 34

Scenes		Image entropy
Digit 8	Fig. 34 (a)	9.6882
	Fig. 34 (b)	8.5043
	Fig. 34 (c)	7.3230
Digit 6	Fig. 34 (d)	9.9020
	Fig. 34 (e)	8.8210
	Fig. 34 (f)	7.2756
Digit 3	Fig. 34 (g)	9.6699
	Fig. 34 (h)	8.5087
	Fig. 34 (i)	7.3315

It is worth noting that since the digit 8 and the digit 6 are next to each other in the imaging scenario of the real-measured system, the extra point on the right side of the digit 8 in Fig. 33(a) is the leftmost point of the digit 6. Additionally, the two extra points on the left side of the digit 6 in Fig. 33(b) are the two rightmost points of the digit 8.

In order to further prove the validity of our proposed method, we choose an additional set of data segments from the real-measured data and process them. In the case of the digit 8, the digit 6, and the digit 3, the SAR images without any compensation is shown in Fig. 34(a), (d), and (g), respectively. Furthermore, after the VE compensation via our proposed method, the SAR images in these three scenarios are shown in Fig. 34(b), (e), and (h), respectively. Finally, after the PGA algorithm, the three final SAR images are shown in Fig. 34(c), (f), and (i), respectively. Additionally, the image entropy of Fig. 34 is shown in Table X. Through the additional set of data segments in the real-measured data, we further demonstrate the effectiveness of our proposed method.

V. CONCLUSION

First, the THz SAR echo signal model including platform high-frequency VE is established. In the proposed signal model, the platform VE can be formulated in the form of the harmonic motion, resulting in introducing the phase error into the received signal. Second, the proposed method is introduced for compensation in the THz SAR imaging, which consists of the VA and the RANSAC algorithm combined with the NLS technique and the minimum-entropy principle. Specifically, the following conditions hold.

1) The VA defined based on the IF characteristics is used for the IF extraction, and it further considers the relationship between the frequency points at adjacent time points based on the maximum value search. Hence, it can extract the IF accurately with noise or in multipoint target imaging scenarios lacking isolated strong scattering points.
2) Then, the RANSAC algorithm is employed for parameter estimation, which can select the inliers and remove the outliers in the estimation process. The NLS technique is performed on the inliers in each iteration of the RANSAC algorithm, and the minimum-entropy principle is used for the best model selection. The RANSAC algorithm combined with the NLS technique and the minimum-entropy principle can reduce the interference of the noise or the platform velocity variation in the parameter estimation process and then obtain focused SAR images.

Finally, the simulation and real-measured experiments explain the performance superiority and validity of our proposed algorithm by contrast with the other two methods (i.e., PSP and NLS).

REFERENCES

[1] Z. Sun, C. Li, X. Gao, and G. Fang, "Minimum-entropy-based adaptive focusing algorithm for image reconstruction of terahertz single-frequency holography with improved depth of focus," *IEEE Trans. Geosci. Remote Sens.*, vol. 53, no. 1, pp. 519–526, Jan. 2015.
[2] B. N. Carnio, K. T. Zawilski, P. G. Schunemann, O. Moutanabbir, and A. Y. Elezzabi, "The coming age of pnictide and chalcogenide ternary crystals in the terahertz frequency regime," *IEEE Trans. Terahertz Sci. Technol.*, vol. 12, no. 5, pp. 433–445, Sep. 2022.
[3] D. Ma et al., "Terahertz wave generation from two-color laser-excited air plasma modulated by bichromatic laser fields," *IEEE Trans. Terahertz Sci. Technol.*, vol. 12, no. 3, pp. 267–273, May 2022.
[4] Y. Nan, X. Huang, X. Gao, and Y. J. Guo, "3-D terahertz imaging based on piecewise constant doppler algorithm and step-frequency continuous-wave signaling," *IEEE Trans. Geosci. Remote Sens.*, vol. 59, no. 8, pp. 6771–6783, Aug. 2021.
[5] W. Wang et al., "Low frequency terahertz induced thermoacoustic signal characteristics and its application in solid-state terahertz transmitter power detection," *IEEE Trans. Terahertz Sci. Technol.*, vol. 12, no. 6, pp. 673–677, Nov. 2022.
[6] M. Gezimati and G. Singh, "Terahertz imaging and sensing for healthcare: Current status and future perspectives," *IEEE Access*, vol. 11, pp. 18590–18619, 2023.
[7] P. Wang, J. Lou, G. Fang, and C. Chang, "Progress on cutting-edge infrared-terahertz biophysics," *IEEE Trans. Microw. Theory Techn.*, vol. 70, no. 11, pp. 5117–5140, Nov. 2022.
[8] M. Yang and D. Zhu, "Efficient space-variant motion compensation approach for ultra-high-resolution SAR based on subswath processing," *IEEE J. Sel. Topics Appl. Earth Observ. Remote Sens.*, vol. 11, no. 6, pp. 2090–2103, Jun. 2018.
[9] S. Shao, H. Liu, L. Zhang, P. Wang, and J. Wei, "Ultrawideband ISAR imaging of maneuvering targets with joint high-order motion compensation and azimuth scaling," *IEEE Trans. Geosci. Remote Sens.*, vol. 60, 2022, Art. no. 5214621.
[10] M. AlShaya, M. Yaghoobi, and B. Mulgrew, "Ultrahigh resolution wide swath MIMO-SAR," *IEEE J. Sel. Topics Appl. Earth Observ. Remote Sens.*, vol. 13, pp. 5358–5368, 2020.
[11] J. Chen, B. Liang, D.-G. Yang, D.-J. Zhao, M. Xing, and G.-C. Sun, "Two-step accuracy improvement of motion compensation for airborne SAR with ultrahigh resolution and wide swath," *IEEE Trans. Geosci. Remote Sens.*, vol. 57, no. 9, pp. 7148–7160, Sep. 2019.
[12] M. Chen, X. Qiu, R. Li, W. Li, and K. Fu, "Analysis and compensation for systematical errors in airborne microwave photonic SAR imaging by 2-D autofocus," *IEEE J. Sel. Topics Appl. Earth Observ. Remote Sens.*, vol. 16, pp. 2221–2236, 2023.
[13] D. Damyanov, T. Kubiczek, K. Kolpatzeck, A. Czylwik, T. Schultze, and J. C. Balzer, "3D THz-TDS SAR imaging by an inverse synthetic cylindrical aperture," *IEEE Access*, vol. 11, pp. 9680–9690, 2023.
[14] C. Wang et al., "An efficient algorithm based on frequency scaling for THz stepped-frequency SAR imaging," *IEEE Trans. Geosci. Remote Sens.*, vol. 60, 2022, Art. no. 5225815.
[15] T. Wang, D. Zhu, and X. Meng, "Implementation of terahertz video SAR imaging based on multi-core DSP," in *Proc. Int. Conf. Signal Image Process.*, 2022, pp. 541–545.
[16] W. Zhaofa, W. Yong, D. Yang, S. Xueyong, and T. Gang, "Novel approach of motion compensation for the terahertz SAR imaging based on measured data," in *Proc. IEEE Int. Geosci. Remote Sens. Symp.*, 2021, pp. 5171–5174.

[17] Z. Huang, Z. He, Z. Sun, and Z. Dong, "Analysis and compensation of vibration error of high frequency synthetic aperture radar," in *Proc. IEEE Int. Geosci. Remote. Sens. Symp.*, 2016, pp. 1138–1141.
[18] Y. Wang, Z. Wang, B. Zhao, and L. Xu, "Compensation for high-frequency vibration of platform in SAR imaging based on adaptive chirplet decomposition," *IEEE Geosci. Remote. Sens. Lett.*, vol. 13, no. 6, pp. 792–795, Jun. 2016.
[19] Z. Wang, Y. Wang, and L. Xu, "Parameter estimation of hybrid linear frequency modulation-sinusoidal frequency modulation signal," *IEEE Signal Process. Lett.*, vol. 24, no. 8, pp. 1238–1241, Aug. 2017.
[20] Z. Wang, Y. Wang, and L. Xu, "Method for high-resolution SAR imaging based on inverse radon transform," in *Proc. IET Int. Radar Conf.*, 2018, pp. 6951–6955.
[21] H. Xia, Q. Chen, Y. Li, C. Fu, and H. Wang, "A high frequency vibration compensation approach in terahertz SAR based on wavelet multi-resolution analysis," in *Proc. China Int. SAR Symp.*, 2018, pp. 1–5.
[22] Y. Li et al., "A novel high-frequency vibration error estimation and compensation algorithm for THz-SAR imaging based on local FrFT," *Sensors*, vol. 20, no. 9, Jan. 2020, Art. no. 2669.
[23] Y. Wang, Z. Wang, B. Zhao, and L. Xu, "Parameters estimation of sinusoidal frequency modulation signal with application in synthetic aperture radar imaging," *J. Appl. Remote Sens.*, vol. 10, no. 2, May 2016, Art. no. 020502.
[24] Y. Wang, Z. Wang, B. Zhao, and L. Xu, "Enhancement of azimuth focus performance in high-resolution SAR imaging based on the compensation for sensors platform vibration," *IEEE Sens. J.*, vol. 16, no. 16, pp. 6333–6345, Aug. 2016.
[25] Z. Hao, J. Sun, and D. Gu, "A novel motion compensation method for high resolution terahertz SAR imaging," in *Proc. 15th Int. Congr. Image Signal Process., Biomed. Eng. Inform.*, 2022, pp. 1–6.
[26] Z. Hao, J. Sun, Q. Li, and T. Shan, "Estimation of high-frequency vibration parameters for airborne terahertz SAR using chirplet decomposition and LS sequential estimators," *Remote Sens.*, vol. 14, Jul. 2022, Art. no. 3416.
[27] S. Shi, C. Li, J. Hu, X. Zhang, and G. Fang, "A high frequency vibration compensation approach for terahertz SAR based on sinusoidal frequency modulation Fourier transform," *IEEE Sens. J.*, vol. 21, no. 9, pp. 10796–10803, May 2021.
[28] S. Chen, Y. Wang, and Y. Zhang, "Compensation for high-frequency vibration of SAR imaging in the terahertz band based on linear chirplet transform and empirical mode decomposition," *IEEE J. Sel. Topics Appl. Earth Observ. Remote Sens.*, vol. 16, pp. 1427–1446, 2023.
[29] Z. Wang, Y. Wang, and L. Xu, "Time-frequency ridge-based parameter estimation for sinusoidal frequency modulation signals," in *Proc. Int. Conf. Commun., Signal Process. Syst.*, 2017, pp. 1375–1380.
[30] B. Peng, X. Wei, B. Deng, H. Chen, Z. Liu, and X. Li, "A sinusoidal frequency modulation Fourier transform for radar-based vehicle vibration estimation," *IEEE Trans. Instrum. Meas.*, vol. 63, no. 9, pp. 2188–2199, Sep. 2014.
[31] Y. Zhao et al., "Vibration error analysis and motion compensation of video synthetic aperture radar," *J. Radars*, vol. 4, no. 2, pp. 230–239, 2015.
[32] X. Zhang, Y. Zhang, and J. Sun, "Effects analysis of helicopter platform vibration on terahertz SAR imaging," *J. Terahertz Sci. Electron. Inf. Technol.*, vol. 16, no. 2, pp. 205–211, Apr. 2018.
[33] I. Djurović, "Viterbi algorithm for chirp-rate and instantaneous frequency estimation," *Signal Process.*, vol. 91, no. 5, pp. 1308–1314, May 2011.
[34] O. Chum and J. Matas, "Optimal randomized RANSAC," *IEEE Trans. Pattern Anal. Mach. Intell.*, vol. 30, no. 8, pp. 1472–1482, Aug. 2008.

Siyu Chen was born in 1999. She received the B.S. degree in electronic information engineering from the Harbin Institute of Technology (HIT), Harbin, China, in 2021. She is currently working toward the Ph.D. degree in information and communication engineering with the HIT, Harbin, China.

Her research interests include signal processing and SAR imaging.

Yong Wang (Senior Member, IEEE) was born in 1979. He received the B.S. and M.S. degrees from the Harbin Institute of Technology (HIT), Harbin, China, in 2002 and 2004, respectively, both in electronic engineering, and the Ph.D. degree in information and communication engineering from the HIT, in 2008.

He is currently a Professor with the Institute of Electronic Engineering Technology, HIT. His research interests include time–frequency analysis of nonstationary signal, radar signal processing, and their application in synthetic aperture radar imaging. He has authored/coauthored more than 130 papers, most of them appeared in the journals of IEEE TRANSACTIONS ON GRS, *IET Signal Processing*, *Signal Processing*, etc.

Prof. Wang was the recipient of the Program for New Century Excellent Talents in University of Ministry of Education of China in 2012, and the Excellent Doctor's Degree nomination Award in China in 2010.